JGR Oceans

RESEARCH ARTICLE
10.1029/2019JC015453

M_2 Internal-Tide Generation in STORMTIDE2

Zhuhua Li[1,2] **and Jin-Song von Storch**[1,3]

[1]Max Planck Institute for Meteorology, Hamburg, Germany, [2]College of Oceanography, Hohai University, Nanjing, China, [3]Center for Earth System Research and Sustainability (CEN), Universitt Hamburg, Hamburg, Germany

Key Points:
- Depth-integrated conversion contains work done at both surface and bottom, with the former being about 1% of the latter
- Internal-tide pressure should be defined as the deviation from the depth-averaged pressure perturbation
- Maximum generation occurs at about 3,000 m depth in the Atlantic, but at about 500 m in the Indo-Pacific

Correspondence to:
J.-S. von Storch,
jin-song.von.storch@mpimet.mpg.de

Citation:
Li, Z., & von Storch, J.-S. (2020). M_2 internal-tide generation in STORMTIDE2. *Journal of Geophysical Research: Oceans*, *125*, e2019JC015453. https://doi.org/10.1029/2019JC015453

Received 9 JUL 2019
Accepted 1 MAY 2020
Accepted article online 11 MAY 2020

Abstract Internal-tide generation has been quantified using both pressure work and energy conversion. When calculating the pressure work from simulated or observed data, the internal-tide pressure has to be decomposed from the full pressure, for which various options exist. We show that the conversion, that has to be derived from the *depth-integrated* energy equations, contains the work done by both the form drag at the bottom and that at the surface, with the latter being about 1% of the former. For calculating the pressure work, the internal-tide pressure identified as the deviation from the depth-averaged pressure perturbation has to be used. We analyzed the work done by the bottom form drag in STORMTIDE2, a concurrent simulation of circulations and tides. As expected, the identified internal-tide pressure reveals the characteristic pressure drop from the windward to the leeward side of an obstacle. The M_2 internal-tide generation in STORMTIDE2 is more strongly controlled by the barotropic tide than by the topographic slope, partly because the tidal velocity can change up to one order of magnitude from the top to the foot of a high ridge within a short distance, a feature only produced by a high-resolution model. Consequently, the intense generation maps the immediate proximities of the summits of high ridges, making the global generation to be strongest near 1,200 m and decreasing drastically below 3,000 m. The depth structure of the generation differs in different basins, which could impact differently on circulations in different basins.

Plain Language Summary Breaking of internal tides provides an important energy source for the oceanic meridional overturning circulation. In this context, it is crucial to fully understand and to accurately estimate the internal-tide generation. So far there exist different expressions for quantifying the internal-tide generation. This paper sorts this out by examining these expressions using equations of motions and STORMTIDE2, a concurrent simulation of circulations and tides. Crucial for the expression is the internal-tide pressure which needs to be identified from the full pressure. We show that the identified internal-tide pressure performs in the way as expected from our understanding of the work done by a form drag. For the M_2 internal tide in STORMTIDE2, the intense generation is located in the proximities of the summits of high obstacles, leading to the stronger generation at roughly 1,200 m than further below. This dependence on depth differs in different ocean basins and can impact the diapycnal mixing and the circulation differently in different basins.

1. Introduction

Internal tides form an important portion of the oceanic internal wave field. Accurately estimating the generation of internal tides is crucial not only for improving our understanding of ocean energetics with internal tides being a major energy source for mixing but also for improving the ocean component of climate models, in which the effect of internal waves on circulation has to be parameterized. For instance, the new parameterization of oceanic internal waves Internal Wave Dissipation, Energy and Mixing (IDEMIX) (Eden & Olbers, 2014; Olbers & Eden, 2013; Pollmann et al., 2017), proposed for developing energetically consistent climate models (Eden, 2016; Eden et al., 2014), requires an accurate estimate of internal-tide generation as one of the main wave sources. To this end, we find in literature different expressions for quantifying internal-tide generation at the ocean bottom. It is not always clear how these expressions are related to each other, both with respect to physical meanings and with respect to relative magnitudes of internal-tide generation obtained from these expressions.

Expressions used to quantify internal tide generation can be grouped into two groups. The first one is based on the expression

$$\mathcal{P} = -\mathbf{U}_H \cdot \left(p^i_{-d} \nabla d\right), \tag{1}$$

where p^i_{-d} is the internal-tide pressure at the ocean bottom $z = -d$, $\mathbf{U}_H = (U, V)$ the horizontal tidal velocity, and ∇ the horizontal differential operator. ∇d measures the slope of the bottom topography. A spatial integral of $p^i_{-d}\nabla d$ is also known as a form drag (see e.g., McCabe & Parker, 2006; Warner & MacCready, 2014). Thus, a time average and a spatial integral of $\mathcal{P}$ describes the mean rate of work done by the form drag induced by an internal tide bottom pressure p^i_{-d}.

Quantifying internal tide generation using $\mathcal{P}$ has a long history and follows two streams, depending on the approach used to determine p^i. In the approach proposed by Bell (1975a) and Bell (1975b) which is further extended by Llewellyn et al. (2002), p^i is obtained by solving the linear wave equations semi-analytically under the assumptions of weak topography and small tidal excursion, without relying on numerical simulations. This approach has been used for the global estimates of internal-tide generation and the modal partitioning by (e.g., Falahat et al., 2014; Nycander, 2005 and Vic et al., 2019). In the other approach, p^i is identified from either observed or simulated pressure perturbations, rather than from semi-analytical solutions. The challenge here is to separate and identify the part of the observed/simulated pressure that can be unambiguously attributed to internal tides. The common practice is to define internal-tide pressure as the derivation from the depth-averaged pressure perturbation, which is known as the baroclinicity condition and proposed by Kunze et al. (2002). However, Kelly et al. (2010) criticized this practice and suggested that the internal-tide pressure should be augmented by an extra term related to free surface movement. Hence, it is not clear how to separate internal-tide pressure from the full pressure when working with observations or a model simulation.

The second group does not rely on any form drag. Instead, internal-tide generation is quantified by the rate of conversion from barotropic energy to baroclinic energy (e.g., Fer et al., 2015; Jalali et al., 2014; Kang & Fringer, 2012; Müller, 2013; Niwa & Hibiya, 2004, 2014; Wang et al., 2016). For a hydrostatic fluid, this rate per unit area is given by

$$\mathcal{C} = \overline{g\rho' W}, \quad \text{with} \quad \overline{(\cdot)} = \int_{-d}^{\eta} \cdot \, dz. \tag{2}$$

In the above equation, g is the gravitational acceleration, ρ' is the density perturbation induced by wave motions, and W is the vertical velocity related to the horizontal tidal velocity $\mathbf{U}_H$, and η is the surface height. $\mathcal{C}$ in equation (2) is determined by a vertical integral of a depth-varying quantity $\rho' W$, rather than by bottom quantities, such as internal tide bottom pressure or bottom topography.

$\mathcal{P}$ and $\mathcal{C}$ describe the internal-tide generation using two different concepts, one based on the physical understanding on work done by a form drag and the other on energy conversion. So far, $\mathcal{P}$ and $\mathcal{C}$ have been estimated mostly independently of each other, even though comparison of estimates based on $\mathcal{C}$ and $\mathcal{P}$ is occasionally also made (e.g., Kang & Fringer, 2012). To our knowledge, it is not clear which one of the expressions ($\mathcal{C}$ or any one of the various versions of $\mathcal{P}$ obtained from differently diagnosed internal-tide pressure) truly quantifies the internal tide generation at the bottom topography. Obviously, the question is closely linked to the problem of how to identify the internal-tide pressure from the full pressure, no matter observed or simulated.

The first goal of this paper is to identify the expression quantifying the internal-tide generation at the bottom from first principles that take the form of a set of equations of motions. We will show that $\mathcal{C}$, which represents the conversion rate of *depth-integrated* energy contains not only the work done by a form drag at the bottom, but also by a form drag at the surface. Moreover, when considering the equations of barotropic and baroclinic (horizontal) velocities, the two form drags appear as terms that couple the two equations. Apart from these coupling terms, the barotropic velocity is determined by the depth-averaged pressure perturbation and the baroclinic velocity by the deviations thereof. With this result, the internal-tide pressure should be identified as the deviation from the depth-averaged pressure perturbation, and the expression based on the work done by such identified internal tide pressure is the one that truly quantifies the bottom internal tide generation.

Note that the estimate based on semi-analytical solutions is considered here as being less accurate, since they are obtained from linear wave equations under the assumptions of weak topography and small tidal excursion. Internal tide generation is considered to be sensitive to near- and super-critical slopes (Zilberman et al., 2009). Even though semi-analytical solutions can also be obtained for idealized super-critical topographic

features by relaxing the assumption of weak topography (Balmforth & Peacock, 2009; Pétrélis et al., 2006), internal-tide generation is expected to be better represented by explicitly resolving the generation process using numerical models with a realistic bottom topography.

The second goal is to evaluate the expressions of internal-tide generation using STORMTIDE2, an updated concurrent simulation of circulations and tides, following the effort led by Arbic et al. (2010) and Müller et al. (2012). STORMTIDE2 is performed with the Max-Planck Institute Ocean Model (MPIOM) at 0.1° horizontal resolution. Although far from being perfect, the oceanic state and the barotropic and internal tides in STORMTIDE2 are by and large realistic (Appendices A and B). A quantification based on such a model simulation is valuable for the following three reasons. First, most of the global estimates based on the work done by the bottom form drag have been derived from the semi-analytical solutions (Falahat et al., 2014; Nycander, 2005; Vic et al., 2019) under the assumptions of weak topography and small tidal excursion, rather than from the internal-tide pressure identified from the full pressure simulated by a general circulation model. It is not a priori clear how the internal-tide generation due to the identified internal-tide pressure is represented in STORMTIDE2 with a realistic topography that can be both sub- and super-critical.

Secondly, most of the previous studies, both those based on semi-analytical solutions (Nycander, 2005; Vic et al., 2019) and those based on energy conversion rate (Fer et al., 2015; Jalali et al., 2014; Kang & Fringer, 2012; Müller, 2013; Niwa & Hibiya, 2014, 2004; Wang et al., 2016), focus on the global/regional amount and the horizontal distribution of the internal tide generation. The vertical distribution of internal-tide generation, which can affect diapycnal mixing and is hence more relevant for the circulation, has drawn little attention. It is noted that the depth-averaged conversion rate does not directly indicate the depth at which internal tide is generated.

Finally, we want to estimate the error made when quantifying M_2 internal tide generation using the depth-integrated energy conversion rate C within the framework of STORMTIDE2. The result that STORMTIDE2 simulates the general circulation and barotropic and baroclinic tides essentially realistically (Appendices A and B) and generates internal tide in a way as expected from our understanding on the work done by the bottom form drag gives some credit for our error estimate.

With these goals in mind, the paper is organized by addressing the following questions:

1. Which expression truly quantifies internal-tide generation at the ocean bottom and how should internal-tide pressure be identified from full pressure?
2. How large is the error when quantifying internal-tide generation using the depth-integrated energy conversion instead of the work done by the bottom form drag within the framework of STORMTIDE2?
3. What are the main properties of M_2 internal tide generation in STORMTIDE2?

After a brief description of the STORMTIDE2 simulation in section 2, sections 3–5 address these three questions one by one. Concluding remarks are given in section 6.

2. The STORMTIDE2 Simulation

The general circulation model used to perform the STORMTIDE2 simulation is identical to that used for STORMTIDE (Müller et al., 2012). It is the tripolar version of the MPIOM (Jungclaus et al., 2006; Marsland et al., 2003) based on the primitive equations, and developed within the framework of the German consortium project STORM (von Storch et al., 2012, 2016). The horizontal resolution is about 0.1°, that is, roughly 11 km at the equator and reducing southward and reaching the minimum grid size of 2.3 km in the very south. There are 40 levels unevenly distributed in the vertical with the layer thickness ranging within 10–70 min the upper 500 m and reaching 500–600 m for the deep ocean (deeper than 4,428 m). A partial cell formulation (Adcroft et al., 1997; Wolff et al., 1997) is used to better represent the bottom topography. The bottom topography is obtained by interpolating the bathymetry data from the NASA Shuttle Radar Topography Mission at a resolution of 30 arc seconds (SRTM30) onto the model grid.

As in STORMTIDE, the complete lunisolar tidal potential is included in the model as a body force to excite the generation of tides (Thomas et al., 2001). This body force is calculated in real time by considering the actual positions of the sun and the moon. Thus, hundreds of tidal constituents are implicitly taken into consideration. To better simulate barotropic tides, in particular, the phases of barotropic tides

(Gordeev et al., 1977), the self-attraction and loading (SAL) effect needs to be considered. In our simulation, it is parameterized following Thomas et al. (2001) with a baroclinic representation of the self-attraction and loading secondary potential.

The STORMTIDE2 simulation is done in a climate mode, in a way similar to the STORM simulation performed with the MPIOM at the same horizontal grid but without the tidal forcing (von Storch et al., 2012; von Storch et al., 2016). It is preceded by a long spin-up run that covers 33 years. The spinup run is driven by the German Ocean Model Intercomparison Project climatology (Röske, 2006). This climatological surface forcing has a daily temporal resolution and is applied repeatedly each year during the integration. The long spin-up ensures that the eddy field reaches a quasi-steady state at the end of spinup (not shown). As for the STORM run, we then switch to the 6 hourly NCEP/NCAR reanalysis-1 (named NCEP forcing, Kalnay et al., 1996) and integrate the model for the period of 1981–2012.

The main difference between the STORMTIDE2 run and the previous STORMTIDE run (Müller et al., 2012) lies in the way how the ocean is forced at the sea surface. In the STORMTIDE run, the ocean is forced by monthly climatological wind stress together with a restoring of sea surface temperature and salinity to monthly climatological values. The surface restoring can damp high-frequency fluctuations. In STORMTIDE2, the ocean is forced as in STORM by 6-hourly NCEP/NCAR forcing in flux form without temperature restoring.

There are other technical differences between STORMTIDE and STORMTIDE2. Being also forced at high frequencies, the ocean in STORMTIDE2 is less stable than that in STORMTIDE, especially in some coastal regions where high tides and storm surge can occur simultaneously, causing the model to crash. To circumvent this problem, the first model layer is increased from 12-min STORMTIDE to 20-min STORMTIDE2. The time step is also reduced from 600 (Müller et al., 2012) to 180 s in the STORMTIDE2 simulation.

Generally, the surface forcing implemented in STORMTIDE2 is more realistic than that used in STORMTIDE. Together with the multi-decadal spin-up run, it becomes worthwhile to evaluate the performance of such a concurrent simulation, which is summarized Appendix A and B.

3. Deriving Internal Tide Generation from First Principles

An expression that truly quantifies internal-tide generation should be derived from first principles represented by a set of equations of motions. Researchers (Carter et al., 2008; Kang & Fringer, 2012; Kelly et al., 2010, Simmons et al., 2004) agree on the general procedure consisting of (a) deriving the depth-integrated energy balance equations for the barotropic and baroclinic motions and (b) identifying internal-tide generation as the term that occurs with the same magnitude but the opposite signs in the two energy equations. Note that the *depth integration* is needed, since otherwise the barotropic energy equation would not be compatible to the baroclinic energy equation. Note also that by considering depth integral, the resulting expression represents, at least in principle, not only the generation at the bottom, but also that occurring throughout the water column up to the surface. Despite the agreement upon the general procedure, quite different expressions have been obtained as pointed out in section 1.

3.1. The Expression Derived from Depth-Integrated Energy Equations

The outcome of the above procedure depends crucially on the decomposition of vertical velocity. Kang and Fringer (2012), detailed in Kang (2010), decompose the three-dimensional velocity $\mathbf{u} = \mathbf{U} + \mathbf{u}'$, rather than just the horizontal component of $\mathbf{u}$, where $\mathbf{u} \equiv (u, v, w)$, $\mathbf{U} \equiv (U, V, W)$, $\mathbf{u}' \equiv (u', v', w')$, and $U = \frac{1}{H}\bar{u}$, $V = \frac{1}{H}\bar{v}$, with $\overline{(\cdot)}$ being the vertical integration defined in equation (2) and $H = \eta + d$. W is defined such that the continuity equation is satisfied by both $\mathbf{U}$ and $\mathbf{u}'$ and furthermore that the boundary conditions of w are satisfied by $W + w'$. This follows that W has the boundary values

$$W_\eta = \frac{\partial \eta}{\partial t} + \mathbf{U}_H \cdot \nabla \eta, \quad at\ z = \eta \tag{3}$$

and

$$W_{-d} = -\mathbf{U}_H \cdot \nabla d, \quad at\ z = -d. \tag{4}$$

These two boundary conditions are important, since they determine the outcome of the depth integration that will be performed to obtain the depth-integrated energy equations. Note that W is a linear function

of z, since $\frac{\partial W}{\partial z} = -\nabla \cdot U_H$ is z-independent. Thus, the vertical velocity w cannot be decomposed into a depth-independent part and a depth-dependent part. Hereafter, "barotropic velocity" and "baroclinic velocity" denote only the horizontal components of $\mathbf{U}$ and $\mathbf{u}'$, $\mathbf{U}_H$ and $\mathbf{u}'_H$, respectively.

In addition to the velocity decomposition, density ρ is decomposed into

$$\rho(x, y, z, t) = \rho_0 + \rho_b(x, y, z) + \rho'(x, y, z, t), \tag{5}$$

where ρ_0 denotes the constant reference density, ρ_b the background density, and ρ' the remaining time-varying density. Such a decomposition assumes that the density field can be decomposed into one that describes the mean circulation ($\rho_0 + \rho_b$) and one that describes time-varying motions (ρ'), including both barotropic and baroclinic motions. Note that equation (5) differs from the density decomposition used by Kang and Fringer (2012), who assume $\rho_b = \rho_b(z)$ since their model doesn't include the mean circulation. Using $\rho_b(x, y, z)$ introduces a coupling term between the energy equation of the mean circulation and that of the time-varying motions. However, this term is irrelevant for the discussion below. The practical implication of equation (5) is that ρ' is derived by subtracting the time-mean density from the full density $\rho(x, y, z, t)$. Given equation (5), the corresponding decomposition of hydrostatic pressure is

$$p = p_0 + p_b(x, y, z) + p'(x, y, z, t), \tag{6}$$

where p_b is hydrostatically related to ρ_b, and p' to ρ' via

$$\frac{\partial p'}{\partial z} = -g\rho'. \tag{7}$$

Since ρ' represents the density related to all time-varying motions, p' enters the equations of the full velocity. One has hence

$$\frac{\partial \mathbf{u}_H}{\partial t} = -\frac{1}{\rho_0}\nabla p' + \ldots \ . \tag{8}$$

Note that in order to highlight the point we want to prove later (i.e., the form drag terms will be canceled by boundary terms in the vertically integrated energy equation when using the velocity decomposition of Kang, 2012), we list here only the relevant terms. All the other terms are not written out explicitly, but denoted by $+\ldots$ for simplicity. In the final vertically integrated energy equations, these terms represent divergences of various fluxes and the energy sink due to various forms of dissipation (Kang, 2010).

To derive the depth-integrated energy equations for barotropic and baroclinic motions, one needs first to derive the equation for $\mathbf{U}_H$ by depth-averaging the equation of $\mathbf{u}_H$. This results in

$$\begin{aligned} \frac{\partial \mathbf{U}_H}{\partial t} &= -\frac{1}{\rho_0 H}\overline{\nabla p'} + \ldots \\ &= -\frac{1}{\rho_0 H}\nabla \overline{p'} + \frac{1}{\rho_0 H}\left(\underbrace{p'_\eta \nabla \eta}_{\mathrm{D}_s} + \underbrace{p'_{-d}\nabla d}_{\mathrm{D}_b}\right) + \ldots \ , \end{aligned} \tag{9}$$

where Leibniz's integration rule is used, p'_η and $p - d'$ indicate p' at the surface and the bottom of the ocean, and D_s and D_b represent the form drag per unit area at the surface and the bottom, respectively. The equation for $\mathbf{u}'_H$ is derived by subtracting the above equation from that of the full velocity $\mathbf{u}_H$:

$$\begin{aligned} \frac{\partial \mathbf{u}'_H}{\partial t} &= -\frac{1}{\rho_0}\nabla p' + \frac{1}{\rho_0 H}\overline{\nabla p'} + \ldots \\ &= -\frac{1}{\rho_0}\nabla p' + \frac{1}{\rho_0 H}\nabla \overline{p'} - \frac{1}{\rho_0 H}\left(\underbrace{p'_\eta \nabla \eta}_{\mathrm{D}_s} + \underbrace{p'_{-d}\nabla d}_{\mathrm{D}_b}\right) + \ldots \end{aligned} \tag{10}$$

It is tempting to think that the form drag terms that occur with opposite signs in equations (9) and (10) determine the conversion between the barotropic and baroclinic energy. This, however, is not the case, since several further steps are still needed to get the depth-integrated energy equations.

First, one needs to get the equation of the kinetic energy of barotropic motions, $E_k = \frac{1}{2}\rho_o(U^2+V^2)$, by multiplying the equation of $\mathbf{U}_H$ with $\rho_0\mathbf{U}_H$:

$$\begin{aligned}\frac{\partial E_k}{\partial t} &= -\frac{1}{H}\mathbf{U}_H\cdot\left(\nabla\overline{p'} - p'_\eta\nabla\eta - p'_{-d}\nabla d\right) + \dots \\ &= -\frac{1}{H}\nabla\cdot(\overline{p'}\mathbf{U}_H) + \frac{1}{H}\overline{p'}\nabla\cdot\mathbf{U}_H + \frac{1}{H}\left(\mathbf{U}_H\cdot(p'_\eta\nabla\eta) + \mathbf{U}_H\cdot(p'_{-d}\nabla d)\right) + \dots\ .\end{aligned}$$

To write $\frac{1}{H}\overline{p'}\nabla\cdot\mathbf{U}_H$ in a flux form, $\frac{\partial p'W}{\partial z}$ is added and subtracted. One finds, making use of equation (7)

$$\begin{aligned}\frac{\partial E_k}{\partial t} &= -\frac{1}{H}\nabla\cdot(\overline{p'}\mathbf{U}_H) + \frac{1}{H}\overline{p'}\nabla\cdot\mathbf{U}_H + \\ &\quad p'\frac{\partial W}{\partial z} - g\rho' W - \frac{\partial p'W}{\partial z} + \frac{1}{H}\left(\mathbf{U}_H\cdot(p'_\eta\nabla\eta) + \mathbf{U}_H\cdot(p'_{-d}\nabla d)\right) + \dots\ ,\end{aligned} \tag{11}$$

Finally, depth-integrating equation (11), thereby making use of $\nabla\cdot\mathbf{U} = 0$, yields

$$\frac{\partial HE_k}{\partial t} = -\nabla\cdot(\overline{p'}\mathbf{U}_H) - \overline{g\rho' W} - (p'W)_\eta + (p'W)_{-d} + \left(\mathbf{U}_H\cdot(p'_\eta\nabla\eta) + \mathbf{U}_H\cdot(p'_{-d}\nabla d)\right) + \dots\ .$$

We see that with the boundary condition equation (4), the power due to the bottom form drag $\mathbf{U}_H\cdot(p-d'\nabla d)$ is canceled by $(p'W)_{-d}$. When furthermore assuming zero atmospheric pressure, $p\eta'$ vanishes. The above equation reduces to

$$\frac{\partial HE_k}{\partial t} = -\nabla\cdot\mathbf{U}_H\overline{p'} - C + \dots \tag{12}$$

Note that the lhs of equation (12) induces a term that is related to η. This term disappears when considering the total (kinetic plus potential) energy of barotropic motions. In the depth-integrated kinetic energy equation of *baroclinic* motions, the form drag term drops out there too for the same reason. One obtains the result of Kang and Fringer (2012) that C is the only term that appears with opposite signs in the equations of barotropic and baroclinic energy.

3.2. Pressure Decomposition

In order to study the relation between the energy conversion rate C and the work done by a form drag, identifying internal-tide pressure is a necessity and discussed below.

Following equation (8), p' affects the horizontal component of the full velocity $\mathbf{u} = \mathbf{U} + \mathbf{u}'$. In order to decompose p' into parts responsible for $\mathbf{U}_H$ and $\mathbf{u}'_H$, respectively, we take a closer look at the equations of $\mathbf{U}_H$ and $\mathbf{u}'_H$, as given in equations (9) and (10). We now decompose p' into a depth average ($\overline{\overline{p'}} = \frac{1}{H}\int_{-d}^{\eta} p'dz$) and the deviation thereof (p''), that is,

$$p' = \overline{\overline{p'}} + p'', \tag{13}$$

in which p'' has a zero depth average. Recalling $H = \eta + d$, equation (9) can be rewritten as

$$\begin{aligned}\frac{\partial\mathbf{U}_H}{\partial t} &= -\frac{1}{\rho_0 H}\nabla H\overline{\overline{p'}} + \frac{1}{\rho_0 H}\left(p'_\eta\nabla\eta + p'_{-d}\nabla d\right) + \dots \\ &= -\frac{1}{\rho_0 H}\left(H\nabla\overline{\overline{p'}} + \overline{\overline{p'}}\nabla\eta + \overline{\overline{p'}}\nabla d\right) + \frac{1}{\rho_0 H}\left(p'_\eta\nabla\eta + p'_{-d}\nabla d\right) + \dots \\ &= -\frac{1}{\rho_0}\nabla\overline{\overline{p'}} + \underbrace{\frac{1}{\rho_0 H}\left(p''_\eta\nabla\eta + p''_d\nabla d\right)}_{\text{coupling term}} + \dots\ .\end{aligned} \tag{14}$$

Similarly, equation (10) can be rewritten as

$$\begin{aligned}\frac{\partial\mathbf{u}'_H}{\partial t} &= -\frac{1}{\rho_0}\nabla p' + \frac{1}{\rho_0}\nabla\overline{\overline{p'}} - \frac{1}{\rho_0 H}\left(p''_\eta\nabla\eta + p''_{-d}\nabla d\right) + \dots \\ &= -\frac{1}{\rho_0}\nabla p'' - \underbrace{\frac{1}{\rho_0 H}\left(p''_\eta\nabla\eta + p''_{-d}\nabla d\right)}_{\text{coupling term}} + \dots\ .\end{aligned} \tag{15}$$

Equations (14) and (15) show that barotropic motions are coupled to baroclinic motions. The coupling is accomplished by p'' that exerts a form drag on the lower boundary and, in exactly the same manner, another one on the upper boundary. Obviously, these drags vanish, when the boundaries are flat. Further, apart from this coupling, the barotropic velocity is determined by the depth-averaged p', $\overline{\overline{p'}}$, and the baroclinic velocity is determined by the deviation thereof, p''.

It is noted that when deriving the depth-integrated kinetic energy equation from equations (14) and (15), rather than from equations (9) and (10) (section 3.1), the power due to the form drag induced by p'' also drops out (The same procedure is used. In particular, $\frac{\partial p'W}{\partial z}$ is added, in order to get a flux form, and then subtracted. The depth integration of $-\frac{\partial p'W}{\partial z}$, that equals $-(p'W)_\eta + (p'W)_{-d}$ is decomposed into two parts using $p' = \overline{\overline{p'}} + p''$. The former can be written as $\overline{\overline{p'}}(-W_\eta + W_{-d})$, or when using the boundary conditions of W, as $\overline{\overline{p'}}(\frac{\partial H}{\partial t} + \nabla \cdot (H\mathbf{U}_h))$, which vanishes according to the depth-integrated continuity equation. The latter leads to a cancellation with the form drag $p''_{-d}\mathbf{U}_H \cdot \nabla d$.). One arrives at the same result that $\mathcal{C}$ appears with opposite signs in the depth-integrated barotropic and baroclinic energy equation.

3.3. Relation Between Energy Conversion Rate and Work Done by Form Drags

As pointed out in section 3.1, even though $\mathcal{C}$ is derived from first principles under the consideration of a rigorous velocity decomposition, $\mathcal{C}$ contains the energy conversion throughout the water column and hence may include contributions other than the generation at the bottom. The following consideration suggests that this is indeed the case and it also provides us the theoretical relation between $\mathcal{C}$ and $\mathcal{P}$.

Based on the hydrostatic approximation (equation (7)), the identities $\frac{\partial p'}{\partial z} = \frac{\partial p''}{\partial z}$ and $\overline{p''} = 0$, and equations (3) and (4), $\mathcal{C}$ can be rewritten as

$$\begin{aligned}\mathcal{C} &= \overline{g\rho' W} = -\overline{\frac{\partial p''}{\partial z} W} = -\overline{\frac{\partial p'' W}{\partial z}} + \overline{p''}\frac{\partial W}{\partial z} \\ &= -(p''W)_\eta + (p''W)_{-d} \\ &= \underbrace{-\left(p''_\eta \frac{\partial \eta}{\partial t} + \mathbf{U}_H \cdot (p''_\eta \nabla \eta)\right)}_{\mathcal{C}_s} \underbrace{-\mathbf{U}_H \cdot (p''_{-d} \nabla d)}_{\mathcal{C}_b}.\end{aligned} \tag{16}$$

Note that writing $\mathcal{C}$ as the sum of $\mathcal{C}_s$ and $\mathcal{C}_b$ is only possible when expressing $\mathcal{C}$ in terms of p'', despite the fact $\frac{\partial p'}{\partial z} = \frac{\partial p''}{\partial z}$. When expressing $\mathcal{C}$ in term of p and following the same steps described in equation (16), one has, in addition to the surface and bottom form-drag terms that are now functions of p', the term $p'\frac{\partial W}{\partial z}$. This term cannot be dropped, since $\overline{p'}$ is not zero. The fact that $\mathcal{C}$ equals the work done by the surface and bottom form drags induced by p'' is consistent with equations (14) and (15), which identify p'' as being responsible for the coupling between the barotropic and baroclinic motions.

Given that the coupling between the barotropic and the baroclinic velocity equations (equations (14) and (15)) is accomplished by the form drags induced by p'' at the surface and the bottom, and that $\mathcal{C}$ includes the effects of the two drags, $\mathcal{C}_s$ and $\mathcal{C}_b$ should be interpreted as representing the internal-tide generation/destruction at the surface and the bottom of the ocean, respectively. We use the term "destruction," since it is not clear whether energy will be transferred at the surface from barotropic to baroclinic motions, or vice verse. Thus, if one wants to identify an expression describing the internal-tide generation at the bottom topography only, $\mathcal{C}_s$ has to be excluded, as pointed out by Kurapov et al. (2003) and Kelly et al. (2010). The remaining $\mathcal{C}_b$ is identical to $\mathcal{P}$ with $p^i = p''$.

3.4. Discussions on the Derivations

We believe that if the same set of equations of motions (e.g., the set of primitive equations) is considered, and furthermore if the same velocity decomposition is chosen, adopting the general procedure (described in the first paragraph of section 3) should lead to one and only one expression for the internal-tide generation within a water column. The two groups of expressions, one relies on a bottom form drag and takes the form of $\mathcal{P}$ and the other does not involves any bottom form drag and takes the form of $\mathcal{C}$, must result either from using different sets of equations of motions or from using different velocity decompositions. The consideration above (section 3.1) suggests that what really matters is the velocity decomposition, not so much the set of equations of motions (i.e., no so much whether it is a simplified set of primitive equations obtained by, for

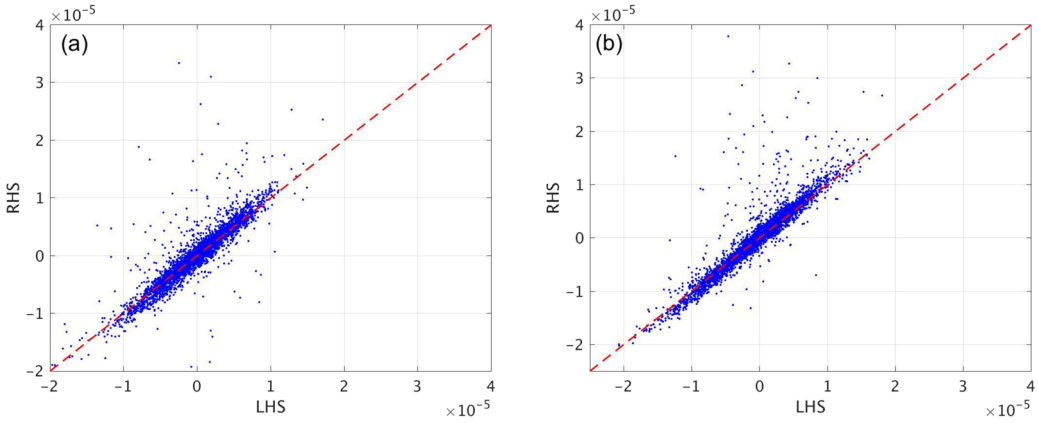

Figure 1. Scatter diagrams of the baroclinic velocity tendency plus the Coriolis term (denoted by LHS) and the gradient of p'' (denoted by RHS), as given in equation (C3) for (a) the zonal and in equation (C4) for (b) the meridional components at one time instance. The unit is m/s^2. The points correspond to values at grid points at 108 m in the Hawaiian Ridge region (see Figure 3a).

example, neglecting the nonlinear advection term or a more complete set obtained by, for example, considering nonhydrostatic pressure). We demonstrate this by showing that the form drag term in the momentum equation is canceled in the depth-integrated energy equation by a boundary term, which arises when using the velocity decomposition suggested by Kang and Fringer (2012). Such a cancellation would not occur if any other velocity decomposition is used.

When using a velocity decomposition different from that of Kang and Fringer (2012), in particular when considering only a decomposition of horizontal velocity without carefully decomposing the vertical velocity (e.g., in Kelly, 2010), the form drag terms in equations (9) and (10) will remain and a power induced by a form drag would occur with opposite signs in the energy equations for barotropic and baroclinic motions, respectively. Since the decomposition by Kang and Fringer (2012) ensures that both the continuity equation and the boundary conditions of w are satisfied, we consider this decomposition as complete and rigorous. However, this is only true in a depth-integrated sense, since C contains the energy conversion throughout the water column.

As shown in section 3.2 $\mathbf{u}'_H$ is determined, apart from a coupling term, by p''. This role of p'' is further verified by examining the relation between $\nabla p''$ and the time rate of change of $\mathbf{u}'_H$ (plus the Coriolis force) away from the boundaries, where the coupling terms (equations (14) and (15)) are not relevant. The consideration follows the formulation given in Appendix C. We find in Figure 1 that at 108 m, which is away from the boundaries, $\nabla p''$ is, by and large, linearly related to the time rate of change of $\mathbf{u}'$ (plus the Coriolis force) at the majority of grid points in the considered region. At the grid points, at which the linear relation is not well satisfied, other terms (e.g., nonlinear advection) in the momentum equation can be relevant. Figure 1 confirms empirically that it is p'' that determines the internal-tide velocity away from the boundaries. Hereafter, p'' is referred to as the identified internal-tide pressure. Using p'' is a widespread practice. It is consistent with the baroclinicity condition proposed by Kunze et al. (2002).

Note also that equation (16) is formally identical to the result obtained when defining internal-tide pressure as the deviation from the depth-averaged pressure perturbation (equations (22) and (23) in Kelly et al. 2010). Kelly et al. (2010) criticized this result and suggested to augment the internal-tide pressure by an extra pressure such that the work done by the form drag at the surface vanishes from their energy equations. In our view, the derivation of the internal-tide generation relies on the *depth-integrated* energy equations so that the resulting expression must contain the work done by both the form drag at the surface and that at the bottom. For quantifying internal tide generation at the bottom, we need only to ignore the work done by the form drag at the surface, rather than to introduce an extra pressure field to eliminate the work done by the surface form drag, as suggested by Kelly et al. (2010). Such an extra pressure field is inconsistent with the equations of barotropic and baroclinic velocity, equations (14) and (15), and furthermore not supported by the empirical evidence shown in Figure 1.

Regarding the question of which expression should be used to quantify the internal-tide generation, we conclude (a) that $C = C_s + C_b$, calculated using p'' at the surface and the bottom, represents the *depth-integrated internal-tide generation/destruction* and (b) that only C_b calculated using p'' at the bottom represents the *internal-tide generation at the bottom*. Note that C_b is identical to $\mathcal{P}$ with $p^i = p''$. Section 4 evaluates the magnitudes of C_b and C_s. Section 5 shows that p''_{-d} indeed performs in the way as expected from the internal-tide bottom form drag.

4. Relative Magnitudes of C_s and C_b

The internal-tide generation is defined by

$$\langle C_b \rangle = -\langle \mathbf{U}_H \cdot (p''_{-d} \nabla d) \rangle, \tag{17}$$

where $\langle \cdot \rangle$ denotes an average over a tidal cycle. For the calculations considered in sections 4 and 5, any variable X that is related to the M_2 barotropic and internal tides (i.e. U, V, or ρ', p'', p''_{-d}) will be represented by the real part of the complex wave ansatz

$$X(x, y, z, t) = a_X(x, y, z) e^{i(\omega t - \phi_X(x,y,z))}, \tag{18}$$

where ω is the M_2 frequency. a_X is referred to as the amplitude and ϕ_X as the phase of X. A detailed description of the calculation of the amplitudes and phases of the identified internal-tide bottom pressure p''_{-d} is given in Appendix D.

The *time mean* rate of work given in equation (17) is proportional to the covariance between the internal-tide bottom pressure and the barotropic tidal velocity. Using the wave ansatz equation (18), the covariances can be written as

$$\langle p''_{-d} \mathbf{U}_H \rangle = (\langle p''_{-d} U \rangle, \langle p''_{-d} V \rangle) = (\frac{1}{2} a_{p''_{-d}} a_U cos(\phi_{p''_{-d}} - \phi_U), \frac{1}{2} a_{p''_{-d}} a_V cos(\phi_{p''_{-d}} - \phi_V)). \tag{19}$$

Equation (17) is thus rewritten as

$$\langle C_b \rangle = \frac{1}{2} \left(a_{p''_{-d}} a_U cos(\phi_{p''_{-d}} - \phi_U) \frac{\partial d}{\partial x} + a_{p''_{-d}} a_V cos(\phi_{p''_{-d}} - \phi_V) \frac{\partial d}{\partial y} \right). \tag{20}$$

Globally integrating $\langle C_b \rangle$ (equation (20)) leads to 0.70 TW M_2-internal-tide generation in the entire ocean. When considering only the generation that is located at depths deeper than 500 m, this number reduces to 0.64 TW. Our estimate of the M_2-internal-tide generation is by and large within the range of the previous studies (and references therein Müller, 2013), but is located in the lower limit.

It should be noted that a direct comparison of our estimate with those obtained by previous studies is extremely difficult. This is not only because different expressions for quantifying the M_2 internal-tide generation are used. More importantly, the difference in the estimates can be caused by the strong sensitivity of the internal-tide generation to the magnitude of the barotropic tide, which differs in different studies. For instance, the estimate provided by Nycander (2005) is based on the tidal velocity field obtained from the TPXO.6 model with a resolution of 1° (Egbert & Erofeeva, 2002). This coarsely resolved velocity field cannot represent the drastic changes in the barotropic tidal velocity shown in Figure 3b, that occurs within a distance as short as 100 km.

In the following, we will concentrate on quantifying the error that is made when diagnosing the internal-tide generation using the depth-integrated energy conversion rate C that contains also the rate of work done by the form drag at the sea surface, C_s. This will be done by comparing $\langle C_b \rangle$ with $\langle C_s \rangle$ within the framework of the STORMTIDE2 simulation.

To estimate $\langle C_s \rangle = -p''_\eta W_\eta$, W_η is calculated using equation (3), and p''_η using the assumption $p'_\eta = 0$. This assumption is consistent with the STORMTIDE2 model, in which the atmospheric pressure is set to zero. With $p'_\eta = 0$, one finds $p''_\eta = p'_\eta - \overline{\overline{p'}} = -\overline{\overline{p'}}$. Even though the magnitude of $\overline{\overline{p'}}$ is often larger than that of p''_{-d}, W_η is much smaller than W_{-d}. Integrated over the entire ocean, $\langle C_s \rangle$ amounts to 0.01 TW, which is about only one percent of the global integral of $\langle C_b \rangle$. Thus, even though C contains the work done by the form drag at the surface, estimating the internal-tide generating using the depth-integrated conversion rate C is quite accurate with the errors amounting to only about 1%.

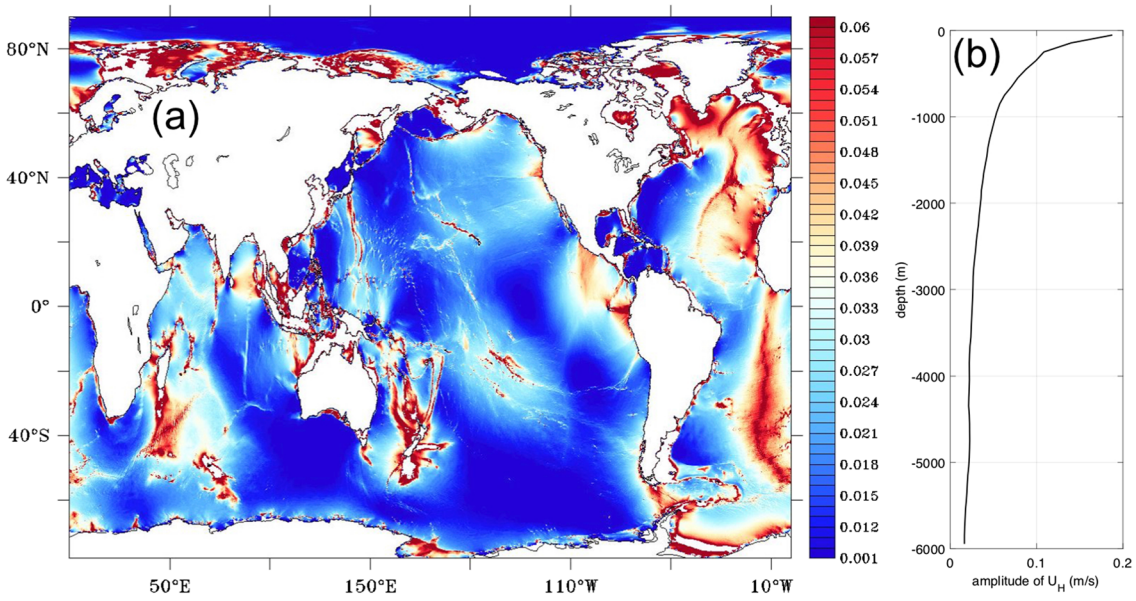

Figure 2. (a) Amplitude of the M_2 barotropic tide, $\sqrt{a_U^2 + a_V^2}$, in m/s for the global ocean. A linear range is used for $0.01 < \sqrt{a_U^2 + a_V^2} < 0.06$. Values larger than 0.1 m/s are indicated by the dark red, and values smaller than 0.001 m/s are indicated by the dark blue. (b) Mean$|\mathbf{U}_H|$ as a function of water depth. The mean $|\mathbf{U}_H|$ at a depth is obtained by averaging $|\mathbf{U}_H|$ in all grid cells that fall within the depth range centered at that depth. The depth range considered have a thickness of 100 m and extend from the surface to 6,000 m.

5. M_2 Internal-Tide Generation in STORMTIDE2

How does the identified internal-tide pressure p'' perform in STORMTIDE2 and what are the properties of the M_2 internal-tide generation in STORMTIDE2? These questions are addressed by evaluating all quantities relevant for the time mean internal-tide generation defined by $\langle C_b \rangle$ in equation (17).

5.1. Horizontal Variations of Barotropic Tide and Topographic Slope

Before considering p'' and the form drag due to p'', this subsection examines the horizontal variations of the barotropic tidal velocity and the topography slope, the two ambient quantities that directly affect the internal-tide generation.

For the M_2 barotropic tide, the amplitude of $\mathbf{U}_H$, as given by $\sqrt{a_U^2 + a_V^2}$ (Figure 2), shows that the M_2 barotropic tidal velocity $\mathbf{U}_H$ has its large magnitude not only along the continental coasts but also away from these coasts over topographic ridges and rises inside the ocean basins. Note that extremely large (larger than 0.1 m/s) and small values (smaller than 0.001 m/s) are indicated by the dark blue and dark red colors. As the water column gets shallower over ridges and rises, the barotropic velocity gets stronger. In order to see this in greater detail, we zoom in into the region over the Hawaiian Ridge northwest of the Hawaii Islands, a region which has been extensively studied (e.g., Carter et al., 2008; Merrifield & Holloway, 2002; Ray & Mitchum, 1996; Zhao, 2018). The respective bathymetry is shown in Figure 3a. This region will also be considered for detailed analysis of other quantities later. Figure 3b shows that large tidal velocities are found over the summits along the Hawaiian Ridge. Moreover, the amplitude of the barotropic velocity changes about one order of magnitude from the foot to the top of the ridge, reaching a maximum speed up to 0.2–0.4 m/s at the summits and a minimum speed down to as low as 0.02 m/s at the foot of the ridge. Such drastic changes occur within less than 100 km. To resolve such tidal velocity changes, a high-resolution ocean model is needed. This conclusion is consistent with the finding by Carter et al. (2008), who showed that a 1-km-resolution simulation has a high level of skill evaluated against observations from moored Acounstic Doppler Current Profilers (ADCPs).

Consider now the barotropic tide over trenches and valleys. Intuitively, one would think that $|\mathbf{U}_H|$ should decrease over trenches and valleys. This is indeed the case, as shown by $|U_H|$ over the Emperor Trench in Figure 4b, with the corresponding bathymetry shown in Figure 4a. $|U_H|$ decreases from about 3.6 cm/s over the summit of the Hess Rise at about 2,500 m depth, to about 1.4 cm/s at the bottom of the Emperor Trench at about 6,000 m depth.

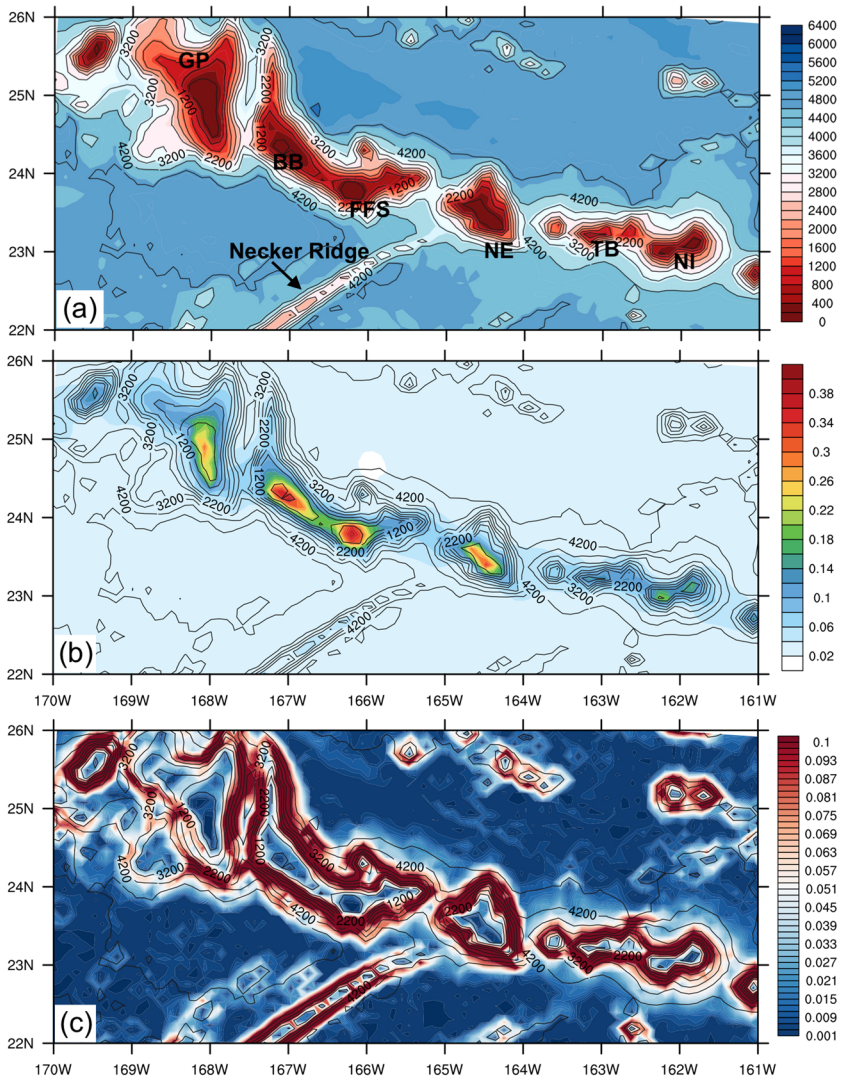

Figure 3. (a) Bottom topography in meters (color shading) for the region over the Hawaiian Ridge northwest of the Hawaiian Islands. Notable topographic features are listed from the west to east: Gardner Pinnaacles (GP), Brooks Banks (BB), French Frigate Shoals (FFS), Necker Island (NE), Twin Banks (TB), and Niihau Island (NI). (b) Amplitude of the M_2 barotropic tide, $\sqrt{a_U^2 + a_V^2}$, in m/s. (c) Magnitude of the bottom slope $|\nabla d|$, with a linear range for $0.005 < |\nabla d| < 0.1$. Values larger than 0.1 are indicated by dark red and those smaller than 0.001 by dark blue. Also shown are isobaths in meters (contours) in all three panels, starting from the shallowest one at 200 m, followed by depths with an increment of 500 m.

Generally, $|\mathbf{U}_H|$ is not a linear function of the water depth. Figure 2b shows the vertical profile of $|\mathbf{U}_H|$ globally averaged over consecutive depth ranges. We can see that $|\mathbf{U}_H|$ reduces with depths, more or less exponentially in the upper 1,000 m, but essentially linearly below 1,500 m. Note that since the majority of trenches are narrow and deep, they can not be well resolved in STORMTIDE2. In particular, our model only considers the water depths until 6,028 m and has a poor vertical resolution in the deep ocean, despite of the use of partial cell. To what extent the horizontal and vertical resolution affects the vertical profile of $|\mathbf{U}_H|$ is not clear.

For the slope, we show in Figure 5 the magnitude of the topographic slope, that is, $|\nabla d| = \sqrt{\frac{\partial d^2}{\partial x} + \frac{\partial d^2}{\partial y}}$. The extremely large values, typically larger than 0.1, are clearly related to narrow ridges, such as the Hawaiian Ridge in the Pacific and the Southwest Indian Ridge in the Indian Ocean. For the region of the Hawaiian Ridge, the maxima of $|\nabla d|$ are located on the slopes to the summits, as shown in Figure 3c. A large-scale feature, which will be used later, is that the magnitudes of topography slope over the Mid-Atlantic Ridge

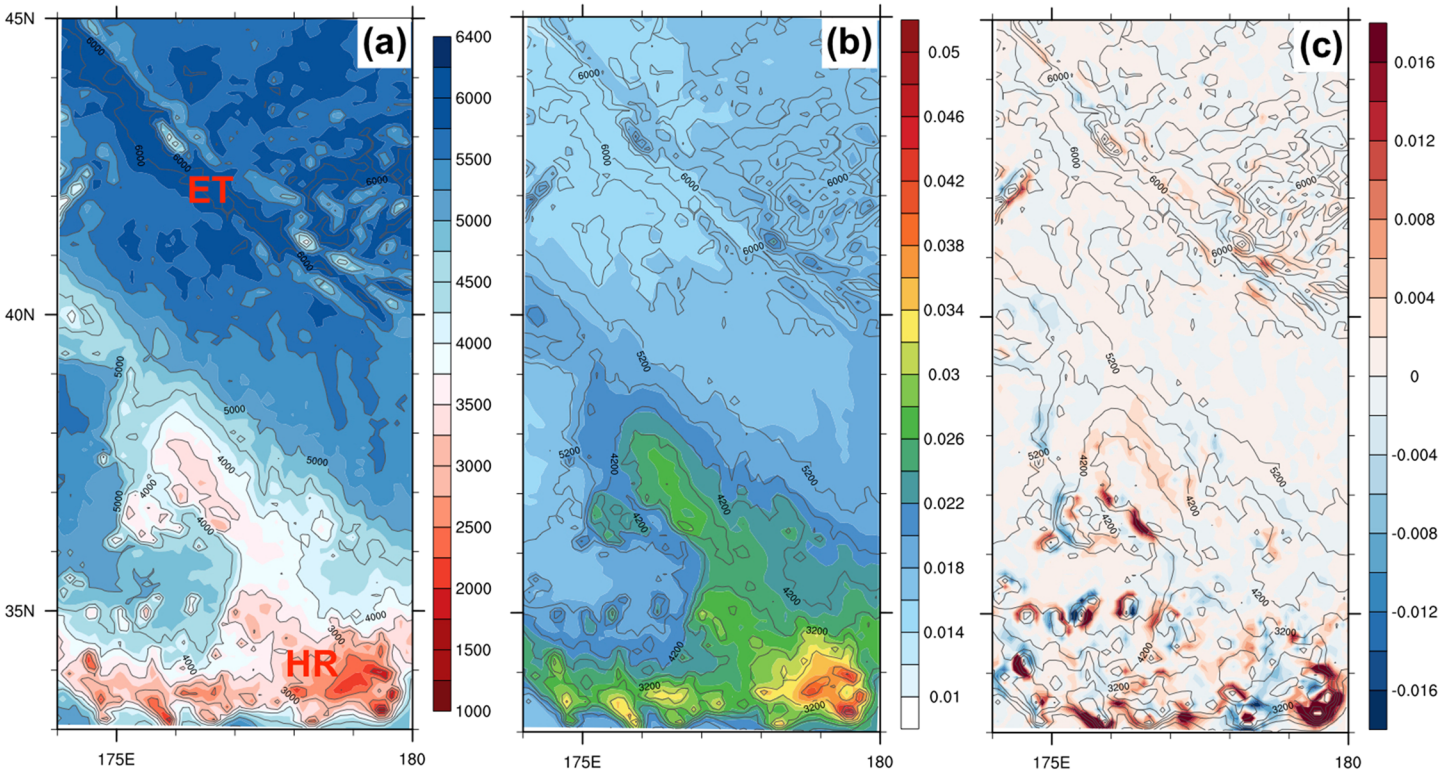

Figure 4. Panels (a) and (b) same as Figures 3a and 3b, but for the region consisting of the Emperor Trough (ET) and the Hess Rise (HR). (c) M_2 internal-tide generation C_b in W/m^2. Also shown are isobaths in meters (contours) in all three panels as in Figure 3.

is comparable to that over the Pacific Antarctic Ridge. They are smaller and located at greater depths than those over the high narrower ridges.

5.2. Amplitude of the Identified Internal-Tide Bottom Pressure

As shown in Figure 6, the most striking feature of the amplitude of the M_2-internal-tide bottom pressure $a_{p''_{-d}}$ is, apart from its small spatial scales of O(100) km, its maxima located over large topographic features. More specifically, one can identify almost all centers of large values of $a_{p''_{-d}}$ with topographic ridges and rises. In the Atlantic, the centers are located over Mid-Atlantic Ridge in the north, and over Rio Grande Rise off the coast of Brazil and Atlantic Ridge in the south. In the Pacific, the centers are located over Sitito Iozima Ridge and West and East Mariana Ridge south of Japan, over the Hawaiian Ridge, in the Region of Archipel des Tuamotu in the central South Pacific, and in the region east of Australia bounded by Lard Howe Rise to the southeast, Colville Ridge to the west, and Indonesia to the north. In the Indian Ocean, the centers are located over the Madagascar Ridge south of Madagascar, the Southwest and Central Indian Ridge east and southeast of Madagascar, over the Melanesie Plateau northeast of Madagascar, and somewhat weaker but still visible over Carlsberg Ridge, and Chagos-Laccadive Ridge surrounding the Arabian Basin. The situation around Maritime Continent is more complex. Also here, centers of large values of $a_{p''_{-d}}$ tend to coincide with underwater rises (not shown). Figure 7 provides a closer look in the region over the Hawaiian Ridge. Shown is p''_{-d} at a time instance of a tidal cycle, at which the magnitude of p''_{-d} is large, which corresponds roughly to $a_{p''_{-d}}$. Large magnitudes of p''_{-d} are located close to the summits along the Hawaiian Ridge. Large magnitudes of p''_{-d} are also found over other considered high ridges and rises in the global ocean.

The magnitude of p''_{-d} is closely related to the barotropic tide and the bottom topography, though to different degrees. This can be seen by comparing the distribution of the amplitude of $a_{p''_{-d}}$ with that of $|\mathbf{U}_H|$ and that of $|\nabla d|$.

Consider first the link to the barotropic tidal velocity. On the regional scales (comparing Figure 7 with Figure 3b), large magnitude of the internal-tide bottom pressure p''_{-d} is found near the summits, where the tidal velocity reaches its maximum. The magnitude of p''_{-d} decreases noticeably further away from the tidal

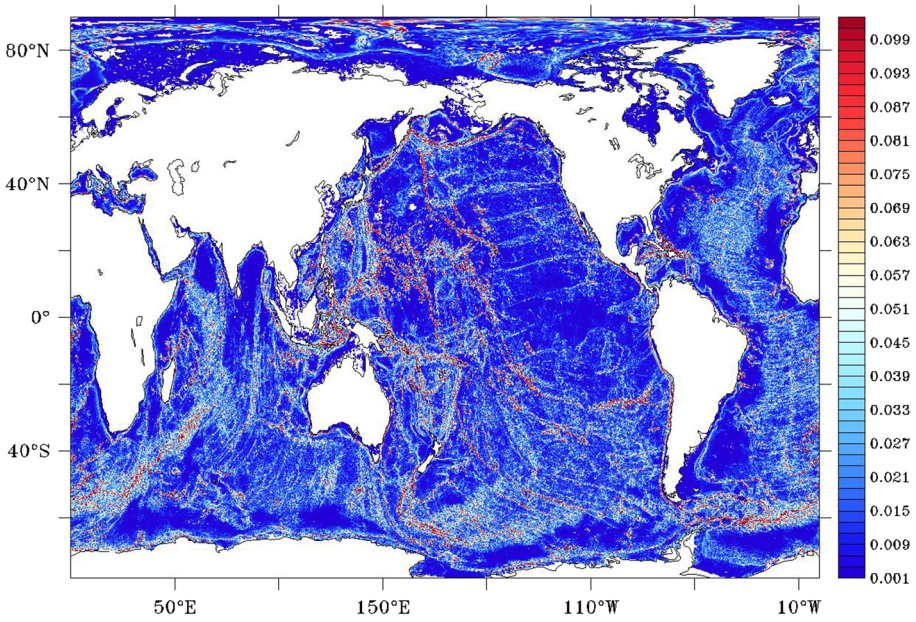

Figure 5. Magnitude of the slope of bottom topography $|\nabla d|$. A linear range is used for $0.005 < |\nabla d| < 0.1$. Values larger than 0.5 are indicated by the dark red; and values smaller than 0.001 are indicated by the dark blue.

velocity maxima. On the basin scales (comparing Figure 6 with Figure 2a), the centers of large values of $a_{p''_{-d}}$ coincide with the locations where the M_2 barotropic tide is strong, and the regions with small values of $a_{p''_{-d}}$ coincide with the regions where the barotropic tide is weak. This is especially the case in the Atlantic, where the strong barotropic tide and large values of $a_{p''_{-d}}$ are found, and in the southern South Pacific and

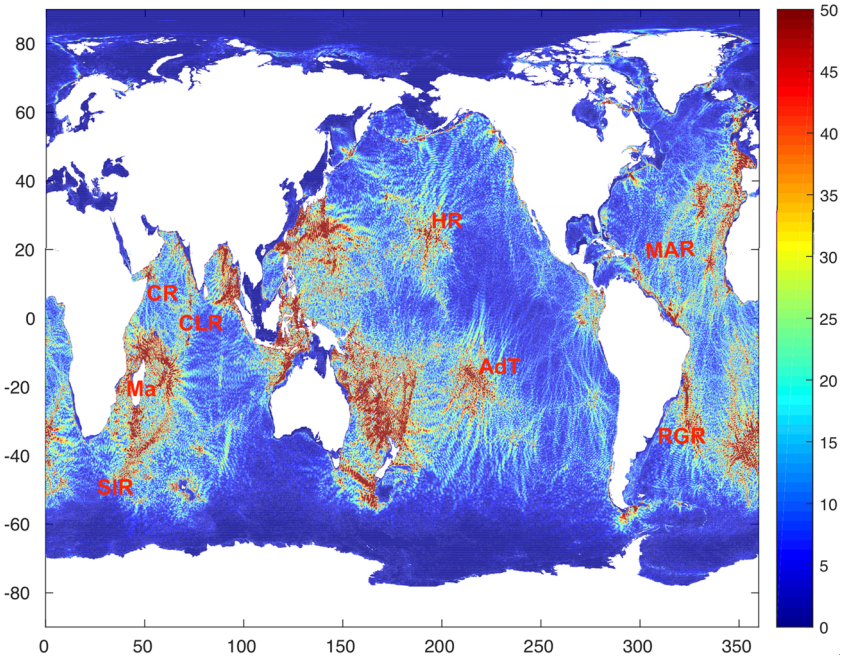

Figure 6. Amplitude of the bottom pressure of the M_2 internal tide, $a_{p''_{-d}}$, in N /m^2. Notable topographic features are labelled from west to east: Southwest Indian Ridge (SIR), Madagascar (Ma), Carlsberg Ridge (CR), Chagos-Laccadive Ridge (CLR), Hawaiian Ridge (HR), Archipel des Tuamotu (AdT), Rio Grande Ridge (RGR), and Mid-Atlantic Ridge (MAR).

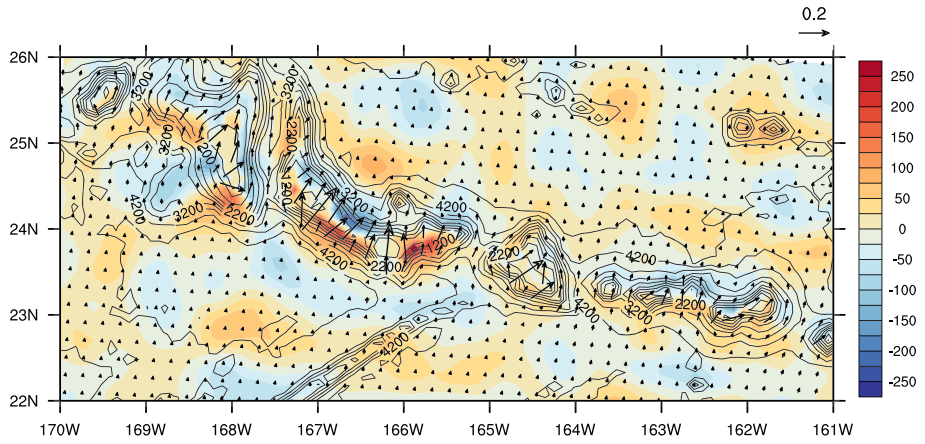

Figure 7. Distribution of instantaneous values of the bottom pressure of the M_2 internal tide p''_{-d} in N/m^2(color shadings) and barotropic M_2 tidal velocity $\mathbf{U}_H$ in m/s (arrows, at every second grid point with $|\mathbf{U}_H| < 0.05$ shown up as arrow head only) for the region over the Hawaiian Ridge. The time instance considered corresponds to the time at which the magnitude of p''_{-d} in the considered region is strong. Also shown are isobaths in meters (contours).

in the southern Indian Ocean east of the Kerguelen Plateau, where the weak barotropic tide and small values of $a_{p''_{-d}}$ are found. One can hence consider the internal-tide bottom pressure as being proportional to the amplitude of the tidal velocity.

This proportionality, however, does not hold unconditionally but depends on the relation between the bottom topography and the direction of the impinging barotropic tide. The proportionality breaks down, when the barotropic tide flows along, rather than perpendicular, to an elongate ridge. The situation can be quantified by the angle between $\mathbf{U}_H$ and ∇d. The proportionality also breaks down at the summit of an obstacle when the tide passes by without impinging on the obstacle. In both cases, no internal-tide pressure is induced.

Consider now the link to topographic slope, which is less clear. For instance, the magnitude of the internal-tide bottom pressure (Figure 6) is smaller in the southern South Pacific than in the South Atlantic, despite the fact that the magnitude of $|\nabla d|$ (Figure 5) in the southern South Pacific is comparable to, and occasionally even larger than that in the South Atlantic. Another example is the Necker Ridge (marked in Figure 3a), where p''_d is weak (Figure 7), even though $|\nabla d|$ is large and $\mathbf{U}_H$ has a notable component perpendicular to the ridge.

Generally, the magnitude of the internal-tide bottom pressure is not, at least not always, proportional to the magnitude of the topographic slope. This result is consistent with the semi-analytical solutions (e.g., Llewellyn et al., 2002), according to which the link of p''_d to $\mathbf{U}_H$ is more direct than that to ∇d, since p''_d at a position is determined not only by ∇d at that position but also by ∇d distant from that position.

5.3. Phase of the Identified Internal-Tide Bottom Pressure

Does the identified internal-tide pressure perform in the way consistent with our understanding on the work done by a bottom form drag that involves a pressure drop from the windward to the leeward side of an obstacle (Miles, 1969; Bell, 1975a)? The answer to this question depends crucially on the phase of p''_{-d} relative to the *direction* of $\mathbf{U}_H$. Figure 7 shows that for the barotropic tide that flows essentially northward at the considered time instance, positive values of p''_{-d} are found on the windward side, and negative ones on the leeward side of the ridges and rises. Thus, the pressure drops from the windward to the leeward of the obstacles. Note that such a pressure drop cannot be diagnosed when considering only the bottom pressure phase without linking this phase to the direction of barotropic tidal velocities.

When expressing p''_{-d} using the wave ansatz (equation (18)), the just described sign change suggests a 180° -shift in phase. Such a phase shift is shown in Figure 8a in the region over the Hawaiian ridge. The phase of p''_{-d} changes from about 200° to 220° (greenish) on the south of the ridge to about 20° to 40° (dark blue) north of the ridge. For a better visualization, the phase variations over a section crossing the Hawaiian Ridge that is roughly in the direction of the semi-major axis (marked by the white line in Figure 8a) is shown in

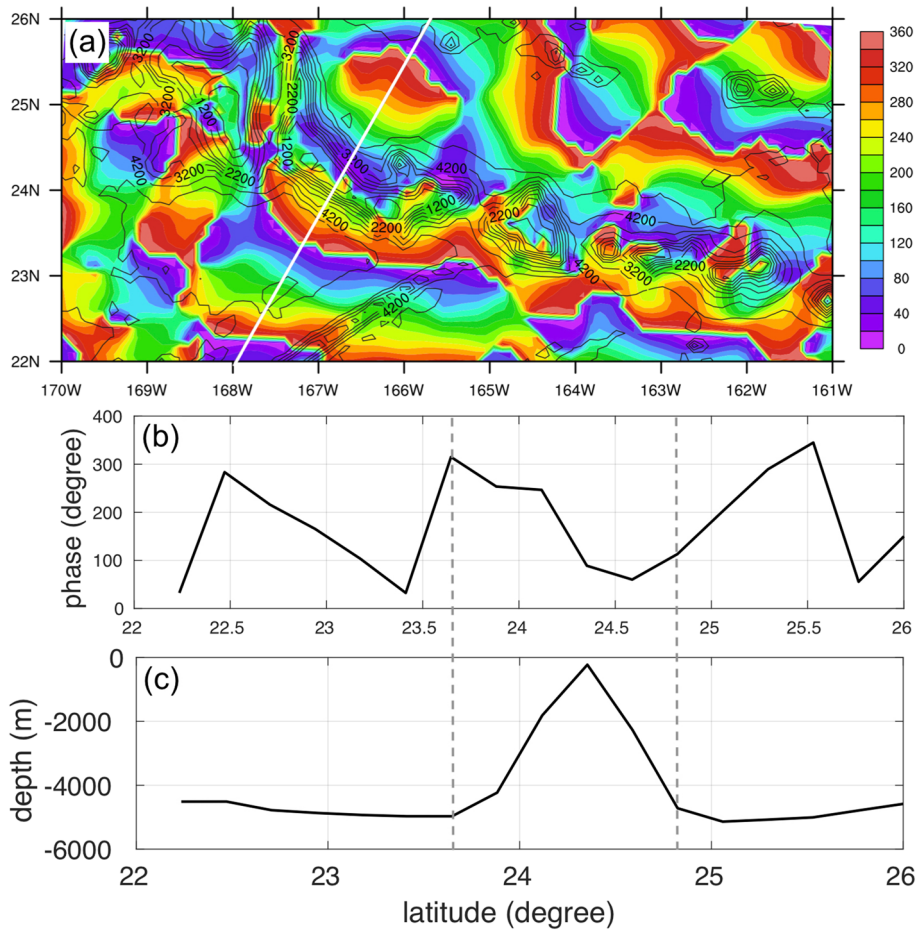

Figure 8. (a) Phase of the M_2-internal-tide bottom pressure p''_d in degrees (color shadings) for the region over the Hawaiian Ridge. Also shown are isobaths in meters (contours). (b) The phase and (c) the topography along the line marked by the white line in (a).

Figure 8b with its related topography in Figure 8c. We can see that the phase changes from about 300° to 100° across the ridge (marked by dashed gray lines), indicating by and large a 180° phase shift. We checked also the other regions with large values of p''_{-d}. The change of p''_{-d} from positive values on one side to negative ones on the other side of an obstacle is systematic and visible over all considered high underwater ridges and rises.

5.4. M_2 Internal-Tide Generation

As shown in equation (19), internal-tide generation is proportional to the covariance between p''_{-d} and $\mathbf{U}_H$ and thus to the cosine of the phase difference between the two (i.e., $cos(\phi_{p''_{-d}} - \phi_U)$ and $cos(\phi_{p''_{-d}} - \phi_V)$. The covariances vanish, when p''_{-d} is 90° out of phase with U and V. Figure 9 shows $cos(\phi_{p''_{-d}} - \phi_U)$ in the region over the Hawaiian Ridge. Similar picture is obtained for $cos(\phi_{p''_{-d}} - \phi_V)$. Since the phase of the tidal velocity (not shown) varies on scales much larger than that of the internal-tide bottom pressure, the spatial distribution of phase differences $\phi_{p''_{-d}} - \phi_U$ resembles that of $\phi_{p''_{-d}}$ shown in Figure 8a. Generally, p''_{-d} is more or less in phase or anti phase with U and V, so that cosine of the phase difference is either close to 1 or close to -1, especially near the summits of the ridges and rises.

Scalar multiplying the covariance vector $\langle p''_{-d}\mathbf{U}_H \rangle$ with ∇d results in internal tide generation $\langle C_b \rangle$ (equation (20)), whose distribution is shown in Figure 10. The distribution is essentially an imprint of all major high underwater ridges and rises. It is much more localized than the distribution of p''_{-d} shown in Figure 6, presumably due to the fact that $\langle C_b \rangle$ represents the internal-tide generation, whereas p''_{-d} in Figure 6 represents the magnitude of the bottom pressure of the generated internal tide that freely propagates and hence covers a much larger area than the area of the generation sites. Zooming in into the region over the

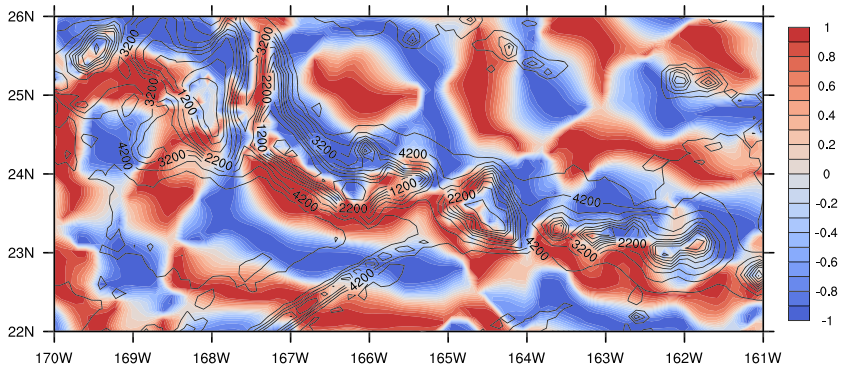

Figure 9. Cosine of the phase difference $\phi_{p_d''} - \phi_U$ for the region over the Hawaiian Ridge. The dark blue and red colors indicate values around ±1, indicating that the phase difference between p_d'' and ϕ_U is about zero or 180° . Also shown are isobaths in meter (contours).

Hawaiian Ridge, Figure 11 shows that the largest internal-tide generation occurs near the summits on the Hawaiian Ridge. A similar picture is also found for $\langle C_b \rangle$ over the other considered high ridges and rises. On the other hand, the internal-tide generation in trenches is generally negligibly weak. In the Emperor Trench region (Figure 4c), C_b is close to zero in the trench. Notable generation (light red) is only found near the small rises by the trench. We checked also several other trenches and found that the generation is negligibly weak in all considered trenches.

Generally, $\mathbf{U}_H$ plays a more dominant role for the internal-tide generation than ∇d does. This is mainly due to the more direct link of internal-tide bottom pressure p_d'' to $\mathbf{U}_H$ as pointed out at the end of section 5.2, which makes C_b in equation (20) roughly quadratic in $|\mathbf{U}_H|$.

5.5. Vertical Structure of Simulated M_2 Internal-Tide Generation

Another feature of the M_2 internal-tide generation is its depth structure in different ocean basins, which can be relevant for the meridional overturning circulations in these basins. The meridional overturning

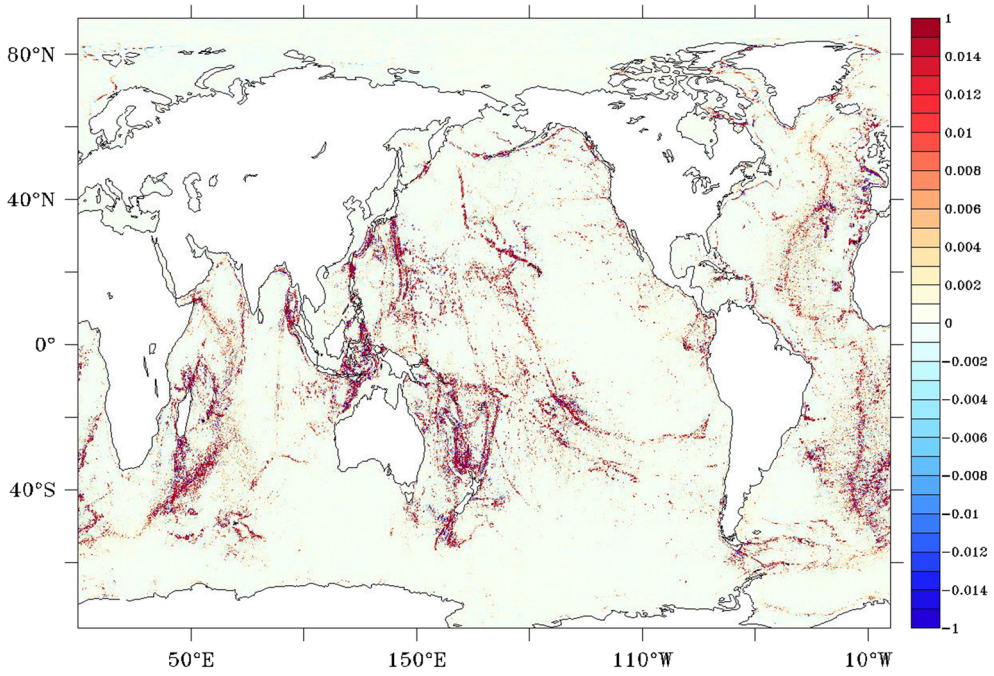

Figure 10. M_2-internal-tide generation C_b in W/m^2 for the global ocean. A linear range is used for $-0.015 < C_b < 0.015$. Values larger than 1 W/m^2 are indicated by the dark red, and values smaller than -1 W/m^2 are indicated by the dark blue. Negative values are mainly found when the magnitude of C_b is small, and are considered to be irrelevant.

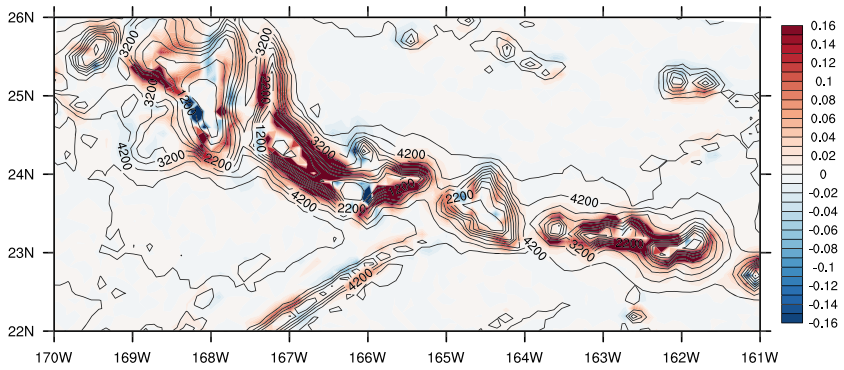

Figure 11. M_2-internal-tide generation C_b in W/m^2 for the region over Hawaiian Ridge.

circulations are strongly controlled by diapycnal mixing induced by wave breaking (Munk & Wunsch, 1998). In this context, not only the intensity but also *the depth* at which the mixing occurs are of crucial importance. Even though STORMTIDE2 cannot explicitly resolve any diapycnal mixing, the simulated vertical structure of the M_2 internal-tide generation can provide some information about the vertical structure of diapycnal mixing related to this internal tide. This is because diapyncal mixing occurs, to a considerable extent, at the generation sites due to breaking of high-mode internal tides (Vic et al., 2019). High modes are generated together with the low modes, which are well resolved by a 0.1° Ocean General Circulation Model (OGCM) (Li et al., 2015). Assuming that a strong generation implies a strong generation of both high and low modes, the vertical structure of low-mode internal-tide generation in a basin, such as that simulated by STORMTIDE2, can reflect the vertical structure of diapycnal mixing due to breaking of internal tides in that basin.

To study the depth structure of internal-tide generation in an ocean basin, we sum up $\langle C_b \rangle$ in all grid cells that fall into the same depth range and normalize the result by the size of the considered basin. The southern boundary of the Atlantic and the Indo-Pacific basin is set at 50° S.

All vertical profiles (Figure 12) reflect the near-summit location of large $\langle C_b \rangle$-values caused by the strong barotropic tides over high ridges and rises. The intense internal-tide generation is not located in the deep ocean, say below 3,000 m. In particular for the global ocean, the largest internal-tide generation is found at about 1,200 m. The generation decreases below 1,200 m, first gradually down to about 3,000 m, and then

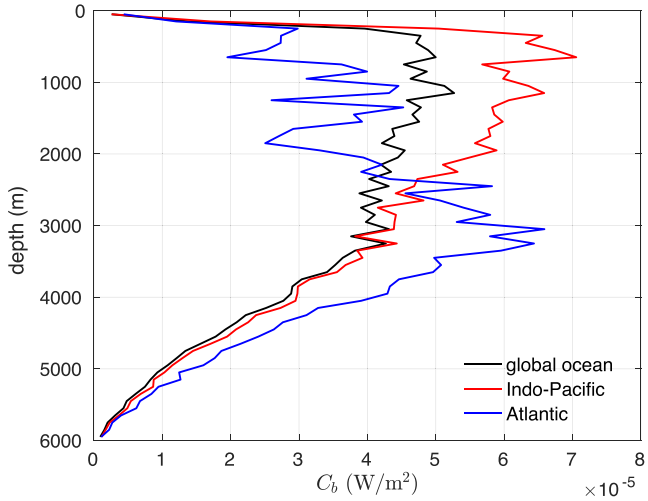

Figure 12. The total M_2-internal-tide generation as a function of the depth of generation sites in the global ocean (black), the Indo-Pacific Ocean (red), and the Atlantic (blue). For each ocean basin, the total generation at a depth is obtained by summing up C_b in all grid cells that fall into the depth range centered at that depth. The depth ranges considered have a thickness of 100 m and extend from the surface to 6,000 m. The total generation is then normalized by the area of the respective basin and hence has the unit of W/m^2.

more drastically down to the deepest part of the global ocean. Note that Figure 12 shows the *total* generation in consecutive depth ranges, normalized by the area of the considered ocean basin. This differs from the depth profile obtained by Buijsman et al. (2016), who considered the *averaged* generation in consecutive depth ranges.

When considering different ocean basins, different depth structures are found. Figure 12 shows that the strongest generation occurs at near 500 m depth in the Indo-Pacific (red line), but at about 3,000 m depth, and hence much deeper, in the Atlantic (blue line). The different depth of the maximum generation is likely caused by the many high narrow ridges in the Indo-Pacific, which lead to the strong shallow generation, and the low broad ridges in the Atlantic, which lead to the strong deep generation. However, the fact that the deep generation in the Atlantic is almost as strong as the shallow generation in the Indo-Pacific, at least when normalized by the the size of the basin, has to be partially attributed to the stronger M_2 barotropic tide in the Atlantic than that in the Indo-Pacific. Note that a stronger M_2 barotropic tide in the Atlantic compared to that in the Indo-Pacific is consistent with the barotropic tides derived from data-assimilated shallow water equations (TPXO.5 Egbert & Ray, 2003).

6. Concluding Remarks

Two different types of expressions have been suggested for quantifying internal-tide generation in literature. One is based on the understanding of the work done by the form drag induced by the internal-tide bottom pressure. The other is based on the depth-integrated conversion rate C between the barotropic and baroclinic energy. So far it is not clear how these two types of expressions are related. Moreover, apart from the approach that derives the internal-tide pressure by semi-analytically resolving the linear wave equations under assumptions, it is not clear how to decompose the pressure such that the internal-tide pressure can be unambiguously identified from the full pressure. Only then, the work done by the form drag can be accurately estimated from observations and model data. The pressure decomposition suggested by Kunze et al. (2002) that internal-tide pressure can be defined as the derivation from the vertically averaged pressure perturbtion is widely used in practice. However, this has been criticized by Kelly et al. (2010) who suggested to augment the internal-tide pressure of Kunze et al. (2002) by an extra pressure that reflects the free surface movement. This paper studies these issues by examining the existing expressions using first principles and by evaluating these expressions using the STORMTIDE2 simulation. The procedure used for the examination is not new. The new aspect is that it is the vertical velocity decomposition used that determines the outcome of the procedure. We find

1. The expression based on the energy conversion C is directly linked to that based on the work done by a form drag. However, since the conversion must be depth-integrated to allow a comparison of the barotropic energy with the baroclinic energy, C contains both the work done by the form drag at the bottom, C_b, and that by the form drag at the surface, C_s. The error induced by the surface form drag is small and only about 1 % of that done by the bottom form drag, at least in STORMTIDE2.
2. The internal-tide pressure should be identified as the deviation from the depth-averaged pressure perturbation, as suggested by Kunze et al. (2002), rather than that as proposed by Kelly et al. (2010). In STORMTIDE2, this is confirmed not only by the clear linear relation between the gradient of this pressure and the time rate of change of the baroclinic velocity (plus the Coriolis force), that is found away from the boundaries, but also by the fact that the form drag due to this pressure shows the characteristic pressure drop from the windward to the leeward side of an obstacle, consistent with our basic understanding on the bottom form drag.

In addition, the analysis based on the STROMTIDE2 simulation suggests also the following features of M_2 internal-tide generation, some of them not explicitly addressed so far.

A. Trenches and valleys do not play the same role as ridges and rises do, with the generation in trenches and valleys being much weaker than that at ridges and rises, at least in STORMTIDE2.
B. The most intense M_2-internal-tide generation maps the immediate proximities of summits of major high underwater ridges and rises, where the tidal velocity is close to its maximum at the summits.
C. Viewed globally, the M_2-internal-tide generation is more intense above than below 1,200 m and decreases drastically below 3,000 m.

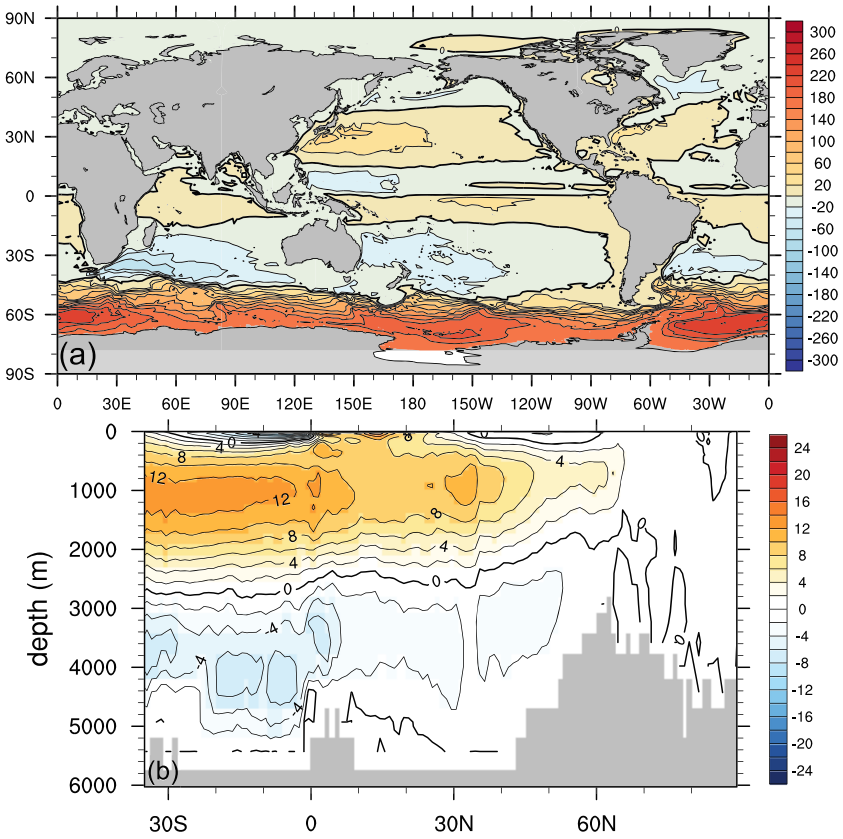

Figure A1. Ten-year-mean (a) barotropic streamfunction (in Sv = 10^6 m^3/s) and (b) Atlantic meridional overturning streamfunction (in Sv).

D. The maximum internal-tide generation is deep and located at about 3,000 min the Atlantic, but shallow and located at about 500 min the Indo-Pacific. This points to the possibility that the Atlantic is heated from below, whereas the Indo-Pacific is heated from above.

All these features are influenced, to different degrees, by the dominance of the barotropic tidal velocity over the topography slope in determining the internal-tide generation, and hence depend strongly on the M_2 barotropic tide velocity simulated by STORMTIDE2.

Appendix A: Basic State in STORMTIDE2

STORMTIDE2 is run using the standard parameterizations (Jungclaus et al., 2006; Jungclaus et al., 2013), without further parameter turning. These parameterizations include a modified PP-scheme (Pacanowski & Philander, 1981) for the description of vertical mixing including that due to surface winds, a bi-harmonic diffusion for momentum dissipation, and a grid-size dependent isopycnal diffusion (Redi, 1982) for horizontal mixing. The parameterization of mesoscale eddies following Gent and McWilliams (1990) is switched off.

The oceanic state is described by averages over the last 10 years of the STORMTIDE2 simulation. The overall distribution of the mean barotropic streamfunction (Figure A1a) is similar to that found in STORM (von Storch et al., 2016), characterized by large-scale gyres and currents systems. The retroflection pattern in the Agulhas region (south of Africa) is captured, as in STORM (von Storch et al., 2016; Jungclaus et al., 2013), due to the high spatial resolution. The simulated Antarctic Circumpolar Current (ACC) shows an evident improvement compared to that in STORM. The overall strength that is unrealistically high in STORM is largely reduced in STORMTIDE2. Specifically, the Drake Passage transport is reduced from over 200 Sv in STORM to about 168 Sv in STORMTIDE2, which is much closer to the observations of 135 ± 20 Sv (Cunningham et al., 2003; Whitworth III & Peterson, 1985). This might be attributed to different mixing in

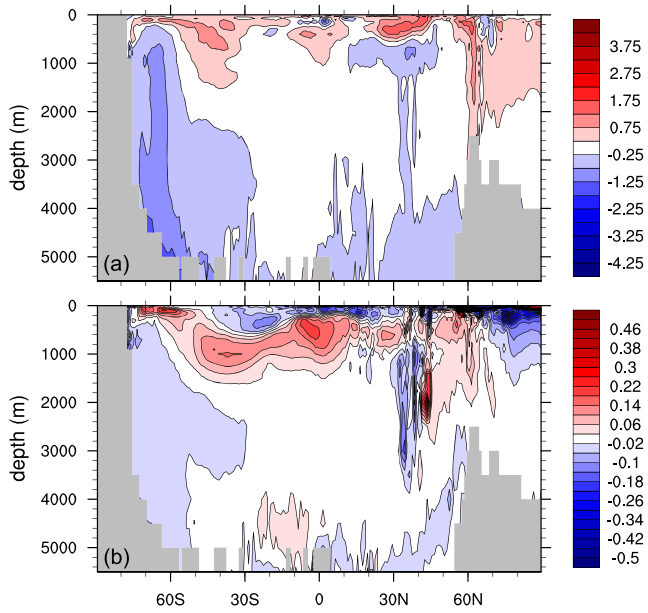

Figure A2. Ten-year-mean zonal-mean (a) temperature and (b) salinity biases relative to PHC (in ° C and mg/kg).

the Southern Ocean, due to near-inertial waves and barotropic and internal tides that are simultaneously resolved in STORMTIDE2.

The mean Atlantic meridional overturning circulation (Figure A1b) reveals two cells with the zero isoline lying between 2,000 and 3,000 m. The upper cell has its location maximum of about 10 Sv near 35° N, much weaker than the respective maximum of about 18 Sv in STORM and the observed value (Cunningham et al., 2007). The bottom cell, indicating the transport of the Antarctic Bottom Water (anti-clockwise) amounts to more than 6 Sv, which is also weaker than that in STORM.

The depth-latitude section of the zonal-mean temperature and salinity biases is shown in Figure A2. The biases are derived relative to Polar Science Center Hydrographic Climatology (Steele et al., 2001), as in von Storch et al. (2016). Similar to the STORM run, the major long-standing warm and saline biases at intermediate water depths (about 200 to 1,500 m) of the low-resolution MPIOM (referring to figures 4 and 5 in von Storch et al., 2016) are largely reduced in STORMTIDE2. The reduction of the mid-depth biases with increasing resolution is attributed to the effect of the resolved eddies (von Storch et al., 2016). The extremely large cold biases of up to about 1.5° C in the region of Antarctic Bottom Water in STORM are reduced down to about 0.75° C in STORMTIDE2, which corrects the strong meridional density gradient and the related strong ACC in STORM. The reduction is accompanied by the warm and saline biases in the upper high-latitude Southern Ocean, which seem to penetrate more downward and northward, leading to larger warm and saline biases at about 1,000 m depth near 50° S–30° S in STORMTIDE2 than in STORM. Generally, the biases are within the range of most of climate models. The stratification in STORMTIDE2 can be considered as being by and large realistic. Further analysis is needed to quantify the role of resolved internal waves for the improved ACC in STORMTIDE2.

Appendix B: Barotropic and Internal Tides in STORMTIDE2

The surface elevation of the last simulation year is analyzed by the least square fitting method of Foreman et al. (2009), from which the harmonic constants of the eight major diurnal and semi-diurnal tidal constituents are derived. These harmonic constants are compared with those of a reference data set at 102 pelagic tide measurements (Shum et al., 1997).

The root-mean-square difference (RMSD) for each tidal constituent is defined as (Stammer et al., 2014)

$$RMSD = \sqrt{\frac{1}{N}\sum_{i=1}^{N}\left(\frac{1}{2}(A_{i,o}^2 + A_{i,m}^2) - A_{i,o}A_{i,m}cos(\phi_{i,o} - \phi_{i,m})\right)}$$

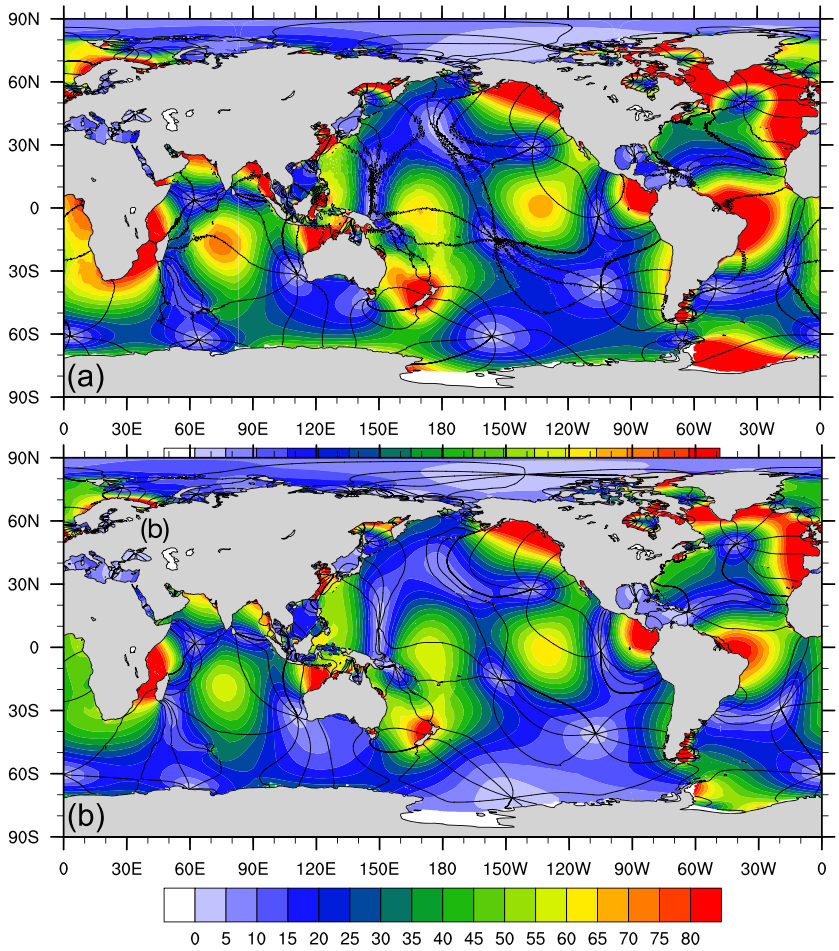

Figure B1. Harmonic constants (color shading for amplitudes in centimeters and contours for phases in degree) of the M_2 tide (a) in the STORMTIDE2 model of the last simulation year and (b) in the HAMTIDE barotropic model.

in which A_o and A_m represent the amplitudes of an individual tidal constituent at the tidal gauge and for the model simulation, respectively. ϕ represents the corresponding phases. $N = 102$ is the total number of the tidal gauges. The signal is computed by $S = \sqrt{\frac{\frac{1}{N}\sum_{i=1}^{N} A_{i,o}^2}{2}}$. The tidal variance captured by the model is indicated by the root-sum-square (RSS)

$$RSS = 1 - \sum_{j=1}^{M} RMSD_j^2 / \sum_{j=1}^{M} S_j^2.$$

The values of S and RMSD are shown in Table B1 for each tidal constituent, with RSS for a total of $M = 8$ tidal constituents considered in the comparison. We can see that the RMSD value of each individual tidal constituent is similar to that of Müller et al. (2012) and Arbic et al. (2004). The RSS is 89.02%, quite close to 92.8% of Müller et al. (2012) and 92.6% of Arbic et al. (2004).

The harmonic constants of the M_2 tide derived from the STORMTIDE2 simulation are shown in Figure B1, comparing with those of the HAMTIDE model, a barotropic data-assimilative model for the global ocean (Zahel, 1995; Taguchi et al., 2014). Note that the HAMITDE model has skills comparable to the widely used TPXO and FES models (Stammer et al., 2014). Differing from the HAMTIDE model (Figure B1b), internal tide signals also show up in the M_2 tide of the STORMTIDE2 model, resulting in small-scale perturbations in both amplitudes and phases (Figure B1a). The comparison shows that the overall patterns resemble each other, and the amplitudes in Figure B1a are in general larger than those of HAMTIDE over the hotspot regions, since the STORMTIDE2 model is not constrained by satellite altimetry data.

Table B1
Tidal Signals, RMS Model Differences against the 102 Gauge Set (Shum et al., 1997) and the RSS Error of the Eight Major Tidal Constituents

	M2	S2	N2	K2	K1	O1	P1	Q1	total
Signal (cm)	33.22	12.62	6.86	3.43	11.26	7.76	3.62	1.62	
RMSD (cm)	10.70	4.94	1.83	1.48	2.34	4.01	0.80	0.88	
RSS (%)									89.02

Abbreviations: RMSD = root-mean-square difference; RSS = root-sum-square.

With a horizontal resolution of 0.1°, the MPIOM model can resolve the first two to three vertical modes of the M_2 internal tide (Li et al., 2015). The kinetic energy of the M_2 internal tide (not shown) has similar spatial distributions at about 100 m and about 1,000 m, with large kinetic energy tightly locked to the bottom topography. The overall structure compares well with the surface signature derived from altimetry data (e.g., Ray & Zaron, 2016; Zhao et al., 2016) and with that derived from STORMTIDE (Li et al., 2015).

Appendix C: Relation Between Baroclinic Velocity and the Identified Internal-Tide Pressure

Neglecting the coupling terms in equation (15), the linear wave momentum equations are given by

$$\frac{\partial u'}{\partial t} - fv' = -\frac{1}{\rho_0}\frac{\partial p''}{\partial x} \tag{C1}$$

$$\frac{\partial v'}{\partial t} + fu' = -\frac{1}{\rho_0}\frac{\partial p''}{\partial y}. \tag{C2}$$

Substituting the real parts of the complex expressions for u' and v', $a_{u'}e^{i(\omega t-\phi_{u'})}$ and $a_{v'}e^{i(\omega t-\phi_{v'})}$, and the real part of the identified internal-tide pressure given in equation (D2) into the above equations, one finds

$$-\omega a_{u'}\sin(\omega t-\phi_{u'}) - fa_{v'}\cos(\omega t-\phi_{v'}) = -\frac{1}{\rho_o}\frac{\partial a_{p''}\cos(\omega t-\phi_{p''})}{\partial x} \tag{C3}$$

$$-\omega a_{v'}\sin(\omega t-\phi_{v'}) + fa_{u'}\cos(\omega t-\phi_{u'}) = -\frac{1}{\rho_o}\frac{\partial a_{p''}\cos(\omega t-\phi_{p''})}{\partial y}. \tag{C4}$$

The relation between the left and right hand sides of equations (C3) and (C4) is shown in Figure 1.

Appendix D: Calculation of the Identified Internal-Tide Pressure p''

Using the wave ansatz given in equation (18), the density perturbation related to the M_2 tides, obtained by applying a harmonic analysis on ρ' in equation (5), is

$$\rho'(x,y,z,t) = a_\rho(x,y,z)e^{i(\omega t-\phi_\rho(x,y,z))}. \tag{D1}$$

With the above perturbation density, the complex representation of the respective hydrostatic pressure perturbation p' is given by

$$p'(x,y,z,t) = p'_z(x,y,z,t) + p'_\eta(x,y,t),$$

where p'_z results from vertically integrating the perturbation density following the hydrostatic relation from z to $z=0$, and p'_η from $z=0$ to $z=\eta$. One finds

$$p'_z(x,y,z,t) = a_{p'}(x,y,z)e^{i(\omega t-\phi_{p'}(x,y,z))}$$

with

$$a_{p'}(x,y,z) = g\left(\left(\int_z^0 a_\rho(x,y,z)\cos(\phi_\rho(x,y,z))dz\right)^2 + \left(\int_z^0 a_\rho(x,y,z)\sin(\phi_\rho(x,y,z))dz\right)^2\right)^{1/2}$$

$$\tan\phi_{p'}(x,y,z)=\frac{\int_z^0 a_\rho(x,y,z)\sin(\phi_\rho(x,y,z))dz}{\int_z^0 a_\rho(x,y,z)\cos(\phi_\rho(x,y,z))dz},$$

and

$$p'_\eta(x,y,t)=a_0(x,y,t)e^{i(\omega t-\phi_0)}$$

with

$$a_0(x,y,t)=ga_\rho(x,y,0)\eta(x,y,t)$$

$$\phi_0(x,y)=\phi_\rho(x,y,0).$$

Thus, when including the contribution p'_η from the sea level height η, p' can no longer be expressed in form of a wave ansatz with time-independent amplitude. Fortunately, the magnitude of surface elevation of O(1) m is already much smaller than the depth of the first model layer of 20 m, so that p'_η can be neglected for p' at the depths of all model layers. In the following, p' is approximated by p'_z with amplitude $a_{p'}$ and phase $\phi_{p'}$ given above, and the depth integral of p' is an integral from $z=-d$ to $z=0$.

The depth average of p' is

$$\frac{1}{d}\overline{p'}(x,y,t)=a_{\overline{p}}(x,y)e^{i(\omega t-\phi_{\overline{p}}(x,y))}$$

with

$$a_{\overline{p}}(x,y)=\frac{1}{d}\left(\left(\int_{-d}^0 a_{p'}\cos\phi_{p'}dz\right)^2+\left(\int_{-d}^0 a_{p'}\sin\phi_{p'}dz\right)^2\right)^{1/2}$$

and

$$\tan\phi_{\overline{p}}(x,y)=\frac{\int_{-d}^0 a_{p'}\sin\phi_{p'}dz}{\int_{-d}^0 a_{p'}\cos\phi_{p'}dz}.$$

The internal-tide pressure p'' obtained by subtracting $\frac{1}{d}\overline{p'}$ from p' is

$$p''(x,y,z,t)=a_{p''}(x,y,z)e^{i(\omega t-\phi_{p''}(x,y,z))} \tag{D2}$$

with

$$a_{p''}(x,y,z)=\left((a_{p'}\cos\phi_{p'}-a_{\overline{p}}\cos\phi_{\overline{p}})^2+(a_{p'}\sin\phi_{p'}-a_{\overline{p}}\sin\phi_{\overline{p}})^2\right)^{1/2}.$$

and

$$\tan\phi_{p''}(x,y,z)=\frac{a_{p'}\sin\phi_{p'}-a_{\overline{p}}\sin\phi_{\overline{p}}}{a_{p'}\cos\phi_{p'}-a_{\overline{p}}\cos\phi_{\overline{p}}}.$$

Acknowledgments
We thank Friederike Pollmann and the two anonymous reviewers for their valuable comments on the manuscript. This paper is a contribution to the project W2 (Energy transfer through low mode internal waves) of the Collaborative Research Centre TRR 181 "Energy Transfer in Atmosphere and Ocean" funded by the Deutsche Forschungsgemeinschaft (DFG, German Research Foundation) - Project number 274762653. This study is also supported by the National Key Research and Development Program of China (Grant 2017YFA0604104) and the Fundamental Research Funds for the Central Universities (Grant 2019B04414). Primary data and scripts used in the analysis that may be useful in reproducing the author's work are archived by the Max Planck Institute for Meteorology and can be obtained by contacting publicationsmpimet.mpg.de upon acceptance.

References

Adcroft, A., Hill, C., & Marshall, J. (1997). Representation of topography by shaved cells in a height coordinate ocean model. *Monthly Weather Review*, *125*, 2293–2315. https://doi.org/10.1175/1520-0493(1997)125<2293:ROTBSC>2.0.CO;2

Arbic, B. K., Garner, S. T., Hallberg, R. W., & Simmons, H. L. (2004). The accuracy of surface elevations in forward global barotropic and baroclinic tide models. *Deep Sea Research II*, *51*, 3069–3101. https://doi.org/10.1016/j.dsr2.2004.09.014

Arbic, B. K., Wallcraft, A. J., & Metzger, E. J. (2010). Concurrent simulation of the eddying general circulation and tides in a global ocean model. *Ocean Modelling*, *32*, 175–187. https://doi.org/10.1016/j.ocemod.2010.01.007

Balmforth, N. J., & Peacock, T. (2009). Tidal conversion by supercritical topography. *Journal of Physical Oceanography*, *39*, 1965–1974. https://doi.org/10.1175/2009JPO4057.1

Bell, T. H. (1975a). Lee waves in stratified flows with simple harmonic time dependence. *Journal of Fluid Mechanics*, *67*, 705–722. https://doi.org/10.1017/S0022112075000560

Bell, T. H. (1975b). Topographically generated internal waves in the open ocean. *Journal of Geophysical Research*, *80*, 320–327. https://doi.org/10.1029/JC080i003p00320

Buijsman, M. C., Ansong, J. K., Arbic, B. K., Richman, J. G., Shriver, J. F., Time, P. G., et al. (2016). Impact of parameterized internal wave drag on semidiurnal energy balance in a global ocean circulation model. *Journal of Physical Oceanography*, *67*, 1399–1419. https://doi.org/10.1175/JPO-D-15-0074.1

Carter, G. S., Merrifield, M. A., Becker, J. M., Katsumata, K., Gregg, M. C., Luther, D. S., et al. (2008). Energetics of M_2 barotropic-to-baroclinic tidal conversion at the Hawaiian islands. *Journal of Physical Oceanography*, *38*, 2205–2223. https://doi.org/10.1175/2008JPO3860.1

Cunningham, S. A., Alderson, S. G., King, B. A., & Brandon, M. A. (2003). Transport and variability of the Antarctic Circumpolar Current in Drake Passage. *Journal of Geophysical Research*, *108*(C5), 8084. https://doi.org/10.1029/2001JC001147

Cunningham, S. A., Kanzow, T., Rayner, D., Baringer, M. O., Johns, W. E., Marotzke, J., et al. (2007). Temporal variability of the Atlantic meridional overturning circulation at 26.5°N. *Science*, *317*, 935–938. https://doi.org/10.1126/science.1141304

Eden, C. (2016). Closing the energy cycle in an ocean model. *Ocean Modelling*, *101*, 30–42. https://doi.org/10.1016/j.ocemod.2016.02.005

Eden, C., Czeschel, L., & Olbers, D. (2014). Toward energetically consistent ocean models. *Journal of Physical Oceanography*, *44*, 3160–3184. https://doi.org/10.1175/JPO-D-13-0260.1

Eden, C., & Olbers, D. (2014). An energy compartment model for propagation, nonlinear interaction, and dissipation of internal gravity waves. *Journal of Physical Oceanography*, *44*, 2093–2106. https://doi.org/10.1175/JPO-D-13-0224.1

Egbert, G., & Erofeeva, S. (2002). Efficient inverse modeling of barotropic ocean tides. *Journal of Atmospheric and Oceanic Technology*, *19*, 183–204.

Egbert, G., & Ray, R. D. (2003). Semi-diurnal and diurnal tidal dissipation from TOPEX/Poseidon altimetry. *Geophysical Research Letters*, *30*(17), 1907. https://doi.org/10.1029/2003GL017676

Falahat, S., Nycander, J., Roquet, F., & Zarroug, M. (2014). Global calculation of tidal energy conversion into vertical normal modes. *Journal of Physical Oceanography*, *44*, 3225–3244. https://doi.org/10.1175/JPO-D-14-0002.1

Fer, I., Müller, M., & Peterson, A. K. (2015). Tidal forcing, energetics, and mixing near the Yermak Plateau. *Ocean Science*, *11*, 287–304. https://doi.org/10.5194/os-11-287-2015

Foreman, M. G. G., Cherniawsky, J. Y., & Ballantyne, V. A. (2009). Versatile harmonic tidal analysis: Improvements and applications. *Journal of Atmospheric and Oceanic Technology*, *26*, 806–817. https://doi.org/10.1175/2008JTECHO615.1

Gent, P. R., & McWilliams, J. C. (1990). Isopycnal mixing in ocean circulation models. *Journal of Physical Oceanography*, *20*, 150–155. https://doi.org/10.1175/1520-0485(1990)020<0150:IMIOCM>2.0.CO;2

Gordeev, R. G., Kagan, B. A., & Polyakov, E. V. (1977). The effects of loading and self-attraction on global ocean tides: The model and the results of a numerical experiment. *Journal of Physical Oceanography*, *7*, 161–170.

Jalali, M., Rapaka, N. R., & Sarkar, S. (2014). Tidal flow over topography: Effect of excursion number on wave energetics and turbulence. *Journal of Fluid Mechanics*, *750*, 259–283. https://doi.org/10.1017/jfm.2014.258

Jungclaus, J. H., Fischer, N., Haak, H., Lohmann, K., Marotzke, J., Matei, D., et al. (2013). Characteristics of the ocean simulations in the Max Planck Institute Ocean Model (MPIOM) the ocean component of the MPI-Earth System Model. *Journal of Advances in Modeling Earth Systems*, *5*, 422–446. https://doi.org/10.1002/jame.20023

Jungclaus, J. H., Keenlyside, N., Botzet, M., Haak, H., Luo, J.-J., Latif, M., et al. (2006). Ocean circulation and tropical variability in the coupled model ECHAM5/MPI-OM. *Journal of Climate*, *19*, 3952–3972. https://doi.org/10.1175/JCLI3827.1

Kalnay, E., Kanamitsu, M., Kistler, R., Collins, W., Deaven, D., Gandin, L., et al. (1996). The NCEP/NCAR 40-year reanalysis project. *Bulletin of the American Meteorological Society*, *77*, 437–472. https://doi.org/10.1175/1520-0477(1996)077<0437:TNYRP>2.0.CO;2

Kang, D. (2010). Energetics and dynamics of internal tides in monterey bay using numerical simulations. Ph.D. dissertation, stanford university, 170 pp. https://stacks.stanford.edu/file/druid:sv691gk5449/kdj_thesis-augmented%.pdf

Kang, D., & Fringer, O. (2012). Energetics of barotropic and baroclinic tides in the Monterey Bay area. *Journal of Physical Oceanography*, *42*, 272–290. https://doi.org/10.1175/JPO-D-11-039.1

Kelly, S. M., Nash, J. D., & Kunze, E. (2010). Internal-tide energy over topography. *Journal of Geophysical Research*, *115*, C06014. https://doi.org/10.1029/2009JC005618

Kunze, E., Rosenfeld, L. K., Carter, G. S., & Gregg, M. C. (2002). Internal waves in Monterey Submarine Canyon. *Journal of Physical Oceanography*, *32*, 1890–1913. https://doi.org/10.1175/1520-0485(2002)032<1890:IWIMSC>2.0.CO;2

Kurapov, A., Egbert, G., Allen, J. S., Miller, R. N., Erofeeva, S. Y., & Kosro, P. M. (2003). The M_2 internal tide off Oregon: Inferences from data assimilation. *Journal of Physical Oceanography*, *33*, 1733–1757. https://doi.org/10.1175/2397.1

Li, Z., von Storch, J.-S., & Müller, M. (2015). The M_2 internal tide simulated by a 1/10° OGCM. *Journal of Physical Oceanography*, *45*, 3119–3135. https://doi.org/10.1175/JPO-D-14-0228.1

Llewellyn, S., Stefan, G., & Young, W. R. (2002). Conversion of the barotropic tide. *Journal of Physical Oceanography*, *32*, 1554–1566. https://doi.org/10.1175/1520-0485(2002)032<1554:COTBT>2.0.CO;2

Marsland, S. J., Haak, H., Jungclaus, J. H., Latif, M., & Röske, F. (2003). The Max-Planck-Institute global ocean/sea ice model with orthogonal curvilinear coordinates. *Ocean Modelling*, *5*, 91–127. https://doi.org/10.1016/S1463-5003(02)00015-X

McCabe, R. M., & Parker, M. (2006). Form drag due to flow separation at a headland. *Journal of Physical Oceanography*, *36*, 2136–2152.

Merrifield, M. A., & Holloway, P. E. (2002). Model estimates of M_2 internal tide energetics at the Hawaiian Ridge. *Journal of Geophysical Research*, *107*, C83179. https://doi.org/10.1029/2001JC000996

Miles, J. W. (1969). Waves and wave drag in stratified flows. In M. Hetenyi, & W. G. Vincenti (Eds.), *Applied mechanics. international union of theoretical and applied mechanics* (pp. 50–76). Berlin, Heidelberg: Springer.

Müller, M. (2013). On the space- and time-dependence of barotropic-to-baroclinic tidal energy conversion. *Ocean Modelling*, *72*, 242–252. https://doi.org/10.1016/j.ocemod.2013.09.007

Müller, M., Cherniawsky, J. Y., Foreman, M. G. G., & von Storch, J.-S. (2012). Global M_2 internal tide and its seasonal variability from high resolution ocean circulation and tide modeling. *Geophysical Research Letters*, *39*, L19607. https://doi.org/10.1029/2012GL053320

Munk, W. H., & Wunsch, C. I. (1998). Abyssal recipes. II: Energetics of tidal and wins mixing. *Deep Sea Research, Part I*, *45*, 1977–2010.

Niwa, Y., & Hibiya, T. (2004). Three-dimensional numerical simulation of M_2 internal tides in the East China Sea. *Journal of Geophysical Research*, *109*, C04027. https://doi.org/10.1029/2003JC001923

Niwa, Y., & Hibiya, T. (2014). Generation of baroclinic tide energy in a global three-dimensional numerical model with different spatial grid resolutions. *Ocean Modelling*, *80*, 59–73. https://doi.org/10.1016/j.ocemod.2014.05.003

Nycander, J. (2005). Generation of internal waves in the deep ocean by tides. *Journal of Geophysical Research*, *110*, C10028. https://doi.org/10.1029/2004JC002487

Olbers, D., & Eden, C. (2013). A global model for the diapycnal diffusivity induced by internal gravity waves. *Journal of Physical Oceanography*, *43*, 1759–1779. https://doi.org/10.1175/JPO-D-12-0207.1

Pacanowski, R. C., & Philander, S. G. H. (1981). Parameterization of vertical mixing in numerical models of tropical oceans. *Journal of Physical Oceanography*, *11*, 1443–1451. https://doi.org/10.1175/1520-0485(1981)011<1443:POVMIN>2.0.CO;2

Pétrélis, F., Llewellyn Smith, S., & Young, W. R. (2006). Tidal conversion at a submarine ridge. *Journal of Physical Oceanography*, *36*, 1053–1071.

Pollmann, F., Carsten, E., & Olbers, D. (2017). Evaluating the global internal wave model IDEMIX using finestructure methods. *Journal of Physical Oceanography*, *47*, 2267–2289. https://doi.org/10.1175/JPO-D-16-0204.1

Ray, R. D., & Mitchum, G. T. (1996). Surface manifestation of internal tides generated near Hawaii. *Geophysical Research Letters*, *23*, 2101–2104. https://doi.org/10.1029/96GL02050

Ray, R. D., & Zaron, E. D. (2016). M_2 internal tides and their observed wavenumber spectra from satellite altimetry. *Journal of Physical Oceanography*, *46*, 3–22. https://doi.org/10.1175/JPO-D-15-0065.1

Redi, M. H. (1982). Oceanic isopycnal mixing by coordinate rotation. *Journal of Physical Oceanography*, *12*, 1154–1158. https://doi.org/10.1175/1520-0485(1982)012<1154:OIMBCR>2.0.CO;2

Röske, F. (2006). A global heat and freshwater forcing dataset for ocean models. *Ocean Modelling*, *11*, 235–297. https://doi.org/10.1016/j.ocemod.2004.12.005

Shum, C. K., Woodworth, P. L., Andersen, O. B., Egbert, G. D., Francis, O., King, C., et al. (1997). Accuracy assessment of recent ocean tide models. *Journal of Geophysical Research*, *102*, 25,173–25,194. https://doi.org/10.1029/97JC00445

Simmons, H. L., Jayne, S. R., St. Laurent, L. C., & Weaver, A. J. (2004). Tidally driven mixing in a numerical model of the ocean general circulation. *Ocean Modelling*, *6*, 245–263. https://doi.org/10.1016/S1463-5003(03)00011-8

Stammer, D., Ray, R. D., Andersen, O. B., Arbic, B. K., Bosch, W., Carrère, L., et al. (2014). Accuracy assessment of global barotropic ocean tide models. *Reviews of Geophysics*, *52*, 243–282. https://doi.org/10.1002/2014RG000450

Steele, M., Morley, R., & Ermold, W. (2001). PHC: A global ocean hydrography with a high-quality Arctic Ocean. *Journal of Climate*, *14*, 2079–2087. https://doi.org/10.1175/1520-0442(2001)014h2079:PAGOHWi2.0.CO;2

Taguchi, E., Stammer, D., & Zahel, W. (2014). Inferring deep ocean tidal energy dissipation from the global high-resolution data-assimilative HAMTIDE model. *Journal of Geophysical Research: Oceans*, *119*, 4573–4592. https://doi.org/10.1002/2013JC009766

Thomas, M., Sündermann, J., & Maier-Reimer, E. (2001). Consideration of ocean tides in an OGCM and impacts on subseasonal to decadal polar motion excitation. *Geophysical Research Letters*, *28*, 2457–2460. https://doi.org/10.1029/2000GL012234

Vic, C., Garabato, A. C. N., Green, J. A. M., Waterhouse, A. F., Zhao, Z., Melet, A., et al. (2019). Deep-ocean mixing driven by small-scale internal tides. *Nature Communications 10*, *2099*, 1–9. https://doi.org/10.1038/s41467-019-10149-5

von Storch, J.-S., Eden, C., Fast, I., Haak, H., Hernández-Deckers, D., Maier-Reimer, E., et al. (2012). An estimate of the Lorenz energy cycle for the world ocean based on the 1/10° STORM/NCEP simulation. *Journal of Physical Oceanography*, *42*, 2185–2205. https://doi.org/10.1175/JPO-D-12-079.1

von Storch, J.-S., Haak, H., Hertwig, E., & Fast, I. (2016). Vertical heat and salt fluxes due to resolved and parameterized meso-scale eddies. *Ocean Modelling*, *108*, 1–19. https://doi.org/10.1016/j.ocemod.2016.10.001

Wang, X., Peng, S., Liu, Z., Huang, R. X., Qian, Y.-K., & Li, Y. (2016). Tidal mixing in the South China Sea: An estimate based on the internal tide energetics. *Journal of Physical Oceanography*, *46*, 107–124. https://doi.org/10.1175/JPO-D-15-0082.1

Warner, S. J., & MacCready, P. (2014). The dynamics of pressure and form drag on a sloping headland: Internal waves versus eddies. *Journal of Geophysical Research: Oceans*, *119*, 1554–1571. https://doi.org/10.1002/2013JC009757

Whitworth III, T., & Peterson, R. G. (1985). Volume transport of the Antarctic Circumpolar Current from bottom pressure measurements. *Journal of Physical Oceanography*, *15*, 810–816. https://doi.org/10.1175/1520-0485(1985)015<0810:VTOTAC>2.0.CO;2

Wolff, J. O., Maier-Reimer, E., & Legutke, S. (1997). The Hamburg Ocean Primitive Equation Model HOPE. German Computer Center (DKRZ).

Zahel, W. (1995). Assimilating ocean tide determined data into global tidal models. *Journal of Marine Systems*, *6*, 3–13. https://doi.org/10.1016/0924-7963(94)00014-3

Zhao, Z. (2018). The global mode-2 M_2 internal tide. *Journal of Geophysical Research: Oceans*, *123*, 7725–7746. https://doi.org/10.1029/2018JC014475

Zhao, Z., Alford, M. H., Girton, J. B., Rainville, L., & Simmons, H. L. (2016). Global observations of open-ocean mode-1 M_2 internal tides. *Journal of Physical Oceanography*, *46*, 1657–1684. https://doi.org/10.1175/JPO-D-15-0105.1

Zilberman, N. V., Becker, J. M., Merrifield, M. A., & Carter, G. S. (2009). Model estimates of M_2 internal tide generation over Mid-Atlantic Ridge topography. *Journal of Physical Oceanography*, *39*, 2635–2651. https://doi.org/10.1175/2008JPO4136.1